

We are IntechOpen, the world's leading publisher of Open Access books Built by scientists, for scientists

6,900

Open access books available

185,000

International authors and editors

200M

Downloads

Our authors are among the

154

Countries delivered to

TOP 1%

most cited scientists

12.2%

Contributors from top 500 universities



WEB OF SCIENCE™

Selection of our books indexed in the Book Citation Index
in Web of Science™ Core Collection (BKCI)

Interested in publishing with us?
Contact book.department@intechopen.com

Numbers displayed above are based on latest data collected.
For more information visit www.intechopen.com



Treatise on Sustainable Infrastructure Construction: Green Composites, Cross Laminated/Mass Timber, Wood Truss Connectors, Nondestructive Technologies, Health Assessment and Monitoring: Utility Poles and Geofoam

Rafaat Hussein

Abstract

The understanding of the engineering performance of green laminated composites is necessary to the design of load bearing components in building and infrastructure construction, and packaging applications. These components are made of outer thin laminae called skins or faces and a thick inner layer called core. The use of bonding is unavoidable in the assembling of these composite products. Like all materials, the bonding materials have finite mechanical properties, e.g. stiffness, but when used in the literature, they are assumed perfectly rigid. That is an unrealistic assumption. Our analytical solutions change this assumption by using the real properties of bonding. In general, the analytical formulations are based on the equilibrium equations of forces, the compatibility of interlaminar stresses and deformation, and the geometrical conditions of the panels. Once solutions are obtained, the next step is to evaluate them. The numerical evaluations proved that perfect rigid bonding in laminated composites greatly underestimates the true performance. At low values of adhesive stiffness, the serviceability is multiple orders of magnitude of that at high values. The logical question is thus: what constitutes perfect bonding? The answer to this question lies in the core-to-adhesive stiffness. The lower the ratio is the higher the error in using the rigid-bond theories. It is worth noting that green-composites in this chapter refer to components made of traditional materials such as wood, in addition to newly developed bio-based and bio-degradable and bio-based composites, made of renewable resources. In addition, bonding and adhesive are used interchangeably.

Keywords: bonding, composites, laminates, rigid-bonding, slip, stiffness

1. Overall introduction

From societal point of view, we must recognize that infrastructure components, such as buildings, represent the physical systems that provide a continual flow of the essential daily services in any society. Their disrepair and degradation disrupt the functioning of business, government, and facilities, as well as have cascading effects throughout the world. Report after report reinforces this prevailing ailing situation. The American Society of Civil Engineers assesses the national status of the infrastructure about each four years. The overall grade point average since 2009 has been around D grade. This is a sign of the needs for urgent actions to repair or replace the ailing systems. The basic challenge is that we must find ways to design new buildings with long life spans so that the annual maintenance required is much



Figure 1.
Overall chapter organization.

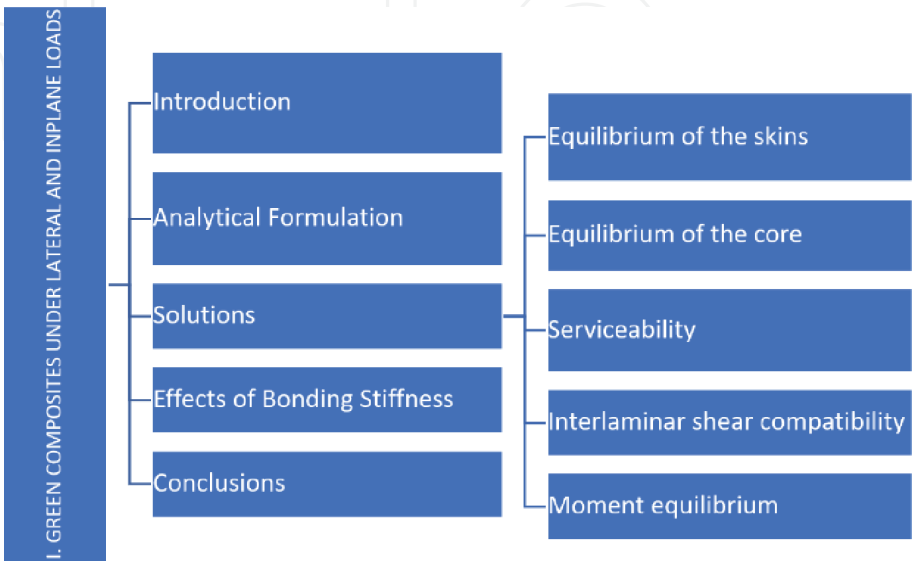


Figure 2.
Part I: Green composites.

less than at present. This chapter is a modern treatise on five practical advances that meet some of the challenges as shown in **Figures 1–6**. Taken as a whole, the chapter brings complex or unsolved problems to everyday practice.

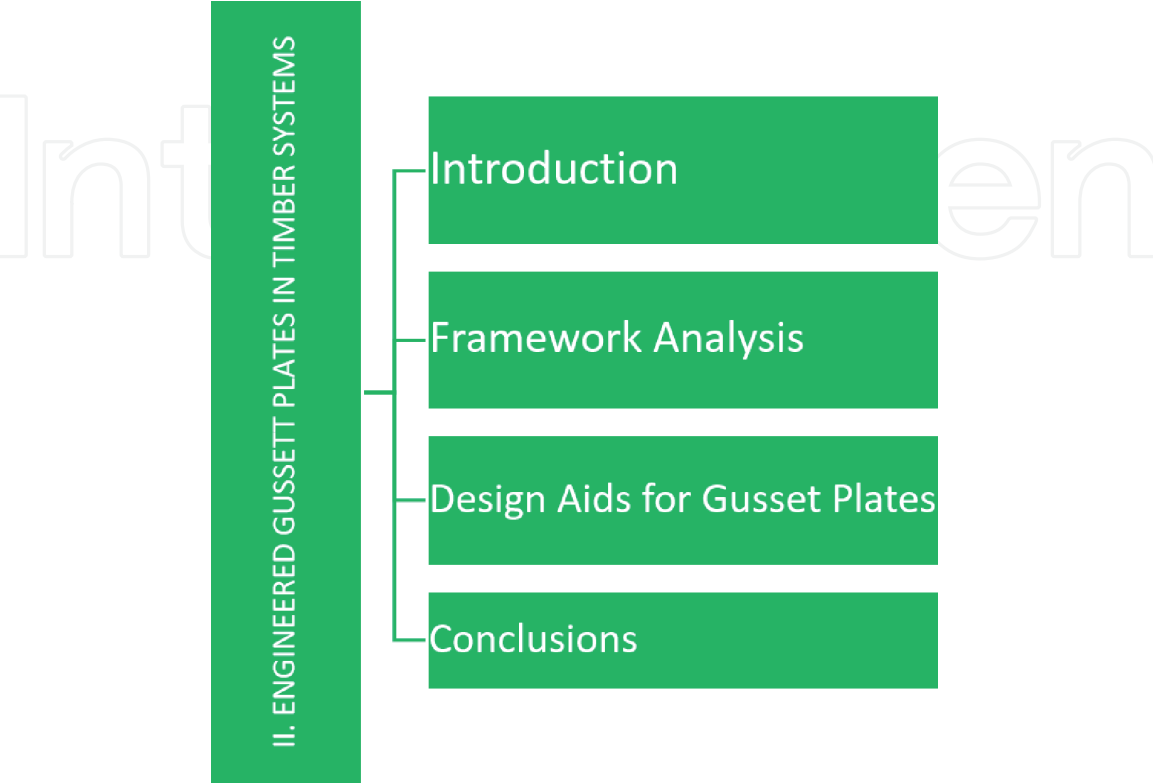


Figure 3.
Engineered Gussett plates in timber systems.

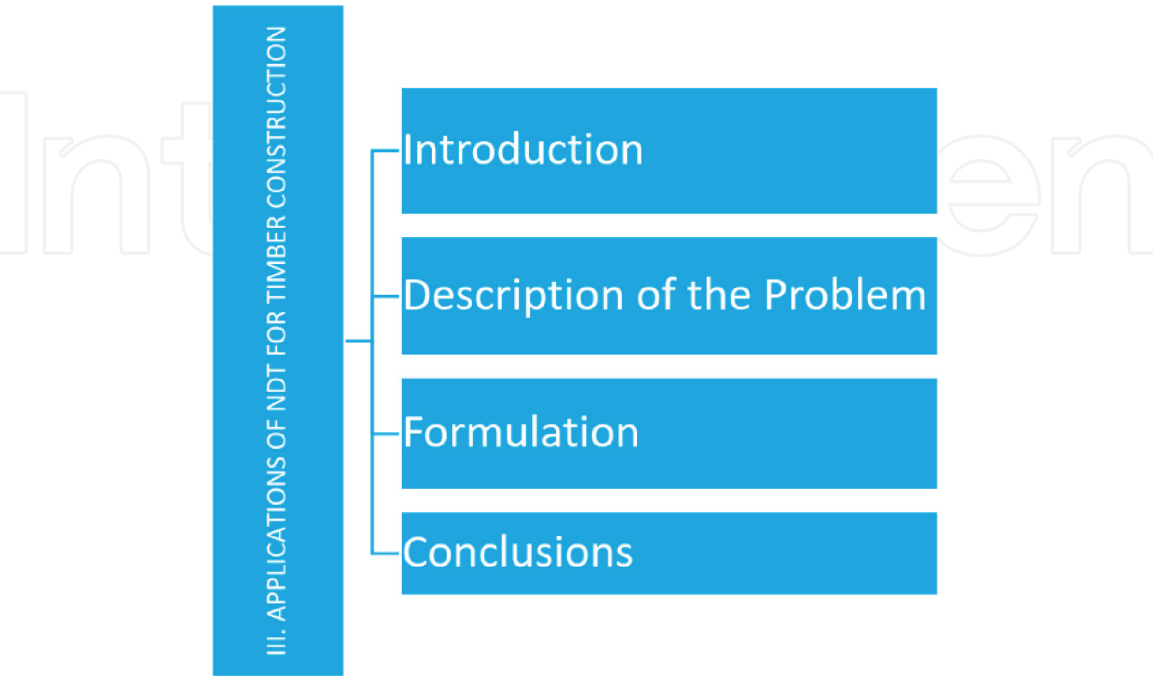


Figure 4.
NDT Technologies for Timber Construction.

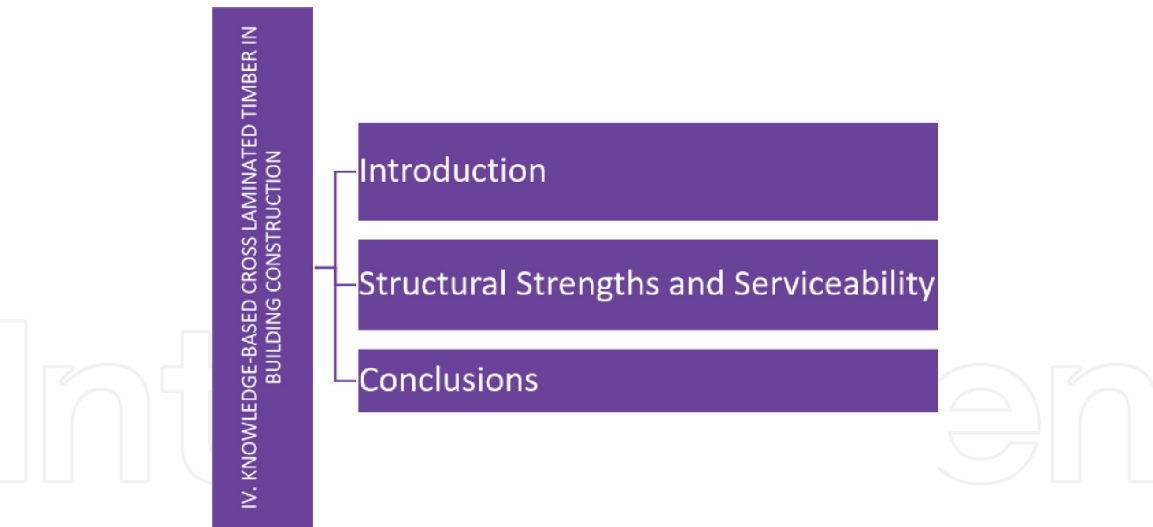


Figure 5.
KB toolkit for CLT.

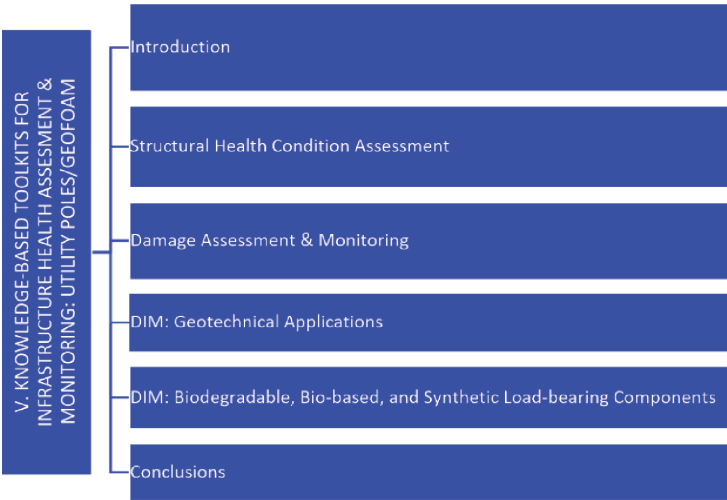


Figure 6.
KB toolkits for utility poles and Geofoam.

2. Green composites under lateral and inplane loads

2.1 Introduction

Laminated composite panels integrate the benefits of each lamina including mechanical and functional properties. In general, the panels are assembled of outer stiff thin layers and an inner thick layer bonded together. The purpose of the face or skin is to carry normal stresses resulting from in-plane and flexural deformations, whereas the core carries shear stresses, keeps the skins apart, and is responsible for the structural integrity of the panel.

The significant advances in the development of green and environmentally friendly materials have placed this type of composites at the forefront of research and development [1–9]. Although laminated composites have been used for over a century, the literature lacks adequate studies on the effects of bonding stiffness on the overall performance. To narrow the gap of the missing information, the author has completed some analytic and experimental studies [4] in this area. This chapter takes the previous studies a step farther. It ascertains the effects of using bonding

materials with finite mechanical properties on the response of the load bearing components in construction. Lateral flexural loads, such as gravity, wind, and pressures, are inevitable in almost all buildings, and packaging applications. In addition, the use of adhesives is also unavoidable for the manufacturing of any laminated composites. The logical question is thus: what affects the realistic adhesive properties, such as stiffness, have on the flexural response of the load bearing panels? The answer to this question provides new knowledge on the true aspects of the structural response and the driving factors. It also narrows the gap in the published articles that assumed perfect rigid bonding layers in laminated composites. Further studies are needed to include damage formation and propagation, localized deformation, and nonlinearity [10–12].

2.2 Analytical formulation

Existing analytic and experimental methods have invariably assumed perfectly rigid bonding between layers [8, 13–15]. Nevertheless, interlaminar delamination occur because of the finite bonding stiffness; the bonds creep under sustained loads, and environmental effects. The high interlaminar shear stress due to applied loads may contribute to an answer of the many delamination in building and infrastructure construction applications. Analysis of wood joist floor systems, commonly used in buildings, including interlaminar shear deformations is available in the literature [8, 16–18]. The wood layers were assembled with nails with glue at their ends. Although the interlaminar deformation in this system was accounted for in the analytical model, transverse shear deformations were neglected. Very few publications deal with the responses of laminated composites with interlaminar deformation or orthotropic material properties. To ascertain the effects of the unrealistic assumption of perfect rigid bonding on the serviceability and strengths of load bearing components in construction, the author has conducted a series of analytical and experimental studies on laminated composites under various loads [14, 19]. The studies used realistic mechanical properties for the bonding materials, introduced in the analytical formulation new parameters such as the core properties, and the in-plane and inter-laminar deformation.

This chapter presents a closed-form solution of laminated composites with interlaminar deformations and under flexural loads. The solution satisfies the equilibrium equations of each lamina and the compatibility of deformations at the interfaces. One of the objectives is to ascertain the effect of interlaminar deformations on the performance of laminates due to transverse flexural loads which are everyday loads in building and infrastructure construction.

2.3 Solutions

The analytic investigation of the laminates at hands is sufficiently mathematically complex due to the existence of non-zero shear and normal strains in the core and bonding. Consider a panel of span $2a$ and width $2b$, as shown in **Figure 7**. The faces are of equal thin thickness t_f . The core of a thickness t_c . The moduli of elasticity of the skins and core are E_f and E_c , respectively. The shear modulus of the core is G_c . The bonding between the laminae has finite stiffness K .

By using the fundamentals of theory of elasticity [19–23], equations are set up to define the equilibrium of the skins and of core elements, and to prescribe the strains continuity between them. The result is a set of differential equations which one solved together lead to the quantities that characterize the overall performance. The stress state in the faces and core elements is shown in **Figure 8**. The equilibrium of the face element requires that

$$\frac{\partial \sigma_{fx}^j}{\partial x} + \frac{\partial \tau_{yx}^j}{\partial y} + \frac{q_x}{t_f^j} = 0 \quad (1)$$

$$\frac{\partial \sigma_{fy}^j}{\partial y} + \frac{\partial \tau_{xy}^j}{\partial x} + \frac{q_y}{t_f^j} = 0 \quad (2)$$

in which σ_{fx} , σ_{fy} , τ_{xy} = normal and shear stress components in the skins;
 q_i = interlaminar shear stress in the i direction ($i = x$ or y); j = superscript denoting stresses in the face j ($j = 1$ bottom skin), x , y = coordinate axes.

The state of stresses in the core must satisfy the following equilibrium equations

$$\frac{\partial \sigma_{cx}}{\partial x} + \frac{\partial \tau_{czz}}{\partial z} = 0 \quad (3)$$

$$\frac{\partial \sigma_{cy}}{\partial y} + \frac{\partial \tau_{czy}}{\partial z} = 0 \quad (4)$$

in which σ_{ci} = normal stress in the skin in the i direction, τ_{czi} = shear stress components in the core. Eqs. 3 and 4 can be written in terms of the displacement components

$$E_{cx} \frac{\partial^2 u_c}{\partial x^2} + G_{cx} \frac{\partial^2 u_c}{\partial z^2} = 0 \quad (5)$$

$$E_{cy} \frac{\partial^2 v_c}{\partial y^2} + G_{cy} \frac{\partial^2 v_c}{\partial z^2} = 0 \quad (6)$$

in which u_c and v_c = displacement in the core along the x and y directions, respectively; E and G = the elastic and shear moduli of the core material.

The stress components in the faces and core must also satisfy the equilibrium equation in terms of the applied load, which is

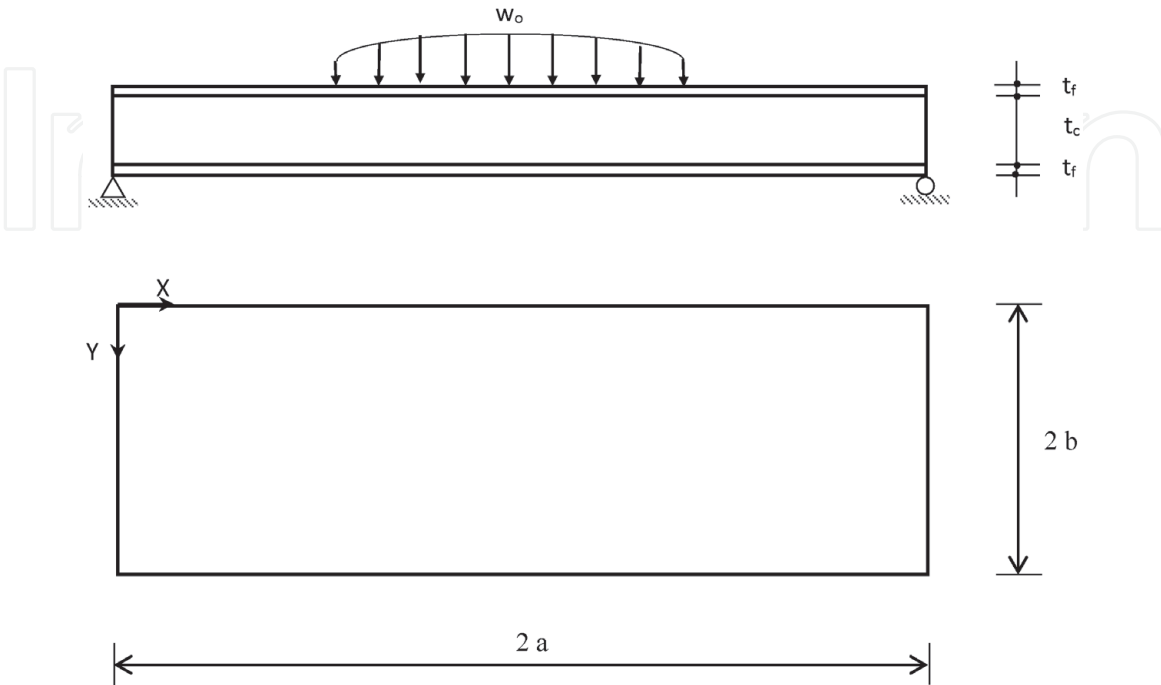


Figure 7.
A typical laminate under transverse load.

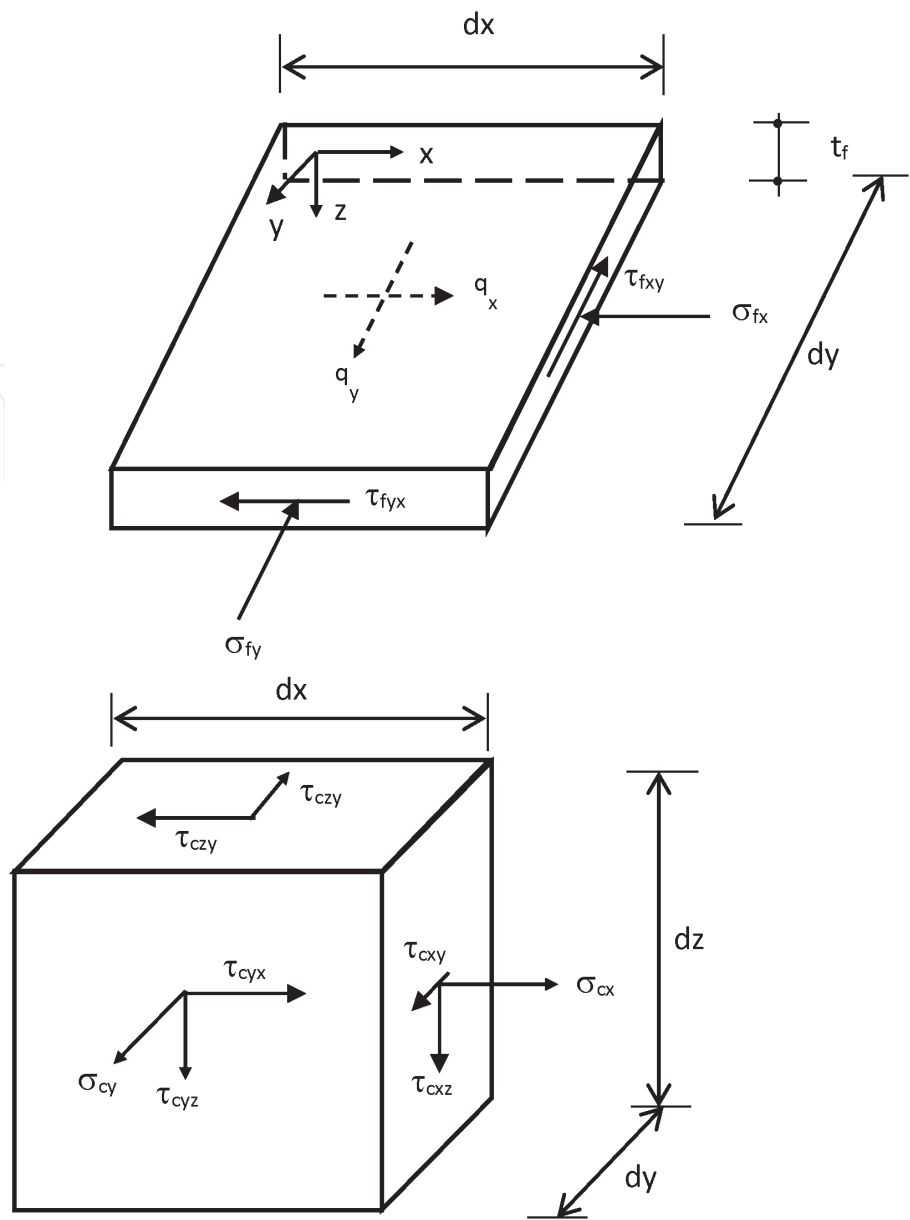


Figure 8.
Stress state in laminates' elements.

$$\frac{\partial^2 M_x}{\partial x^2} - 2 \frac{\partial^2 M_{xy}}{\partial x \partial y} + \frac{\partial^2 M_y}{\partial y^2} = -p \quad (7)$$

in which M_x , M_y ; and M_{xy} = the applied moments; and p = the applied load intensity.

At the interfaces between the core and the skins, the stresses and strains must be compatible. The compatibility equations in terms of stresses are

$$q_x = G_{cx} \left(\frac{\partial u_c}{\partial z} + \frac{\partial \omega}{\partial x} \right)_{z=\frac{1}{2}t_c} \quad (8)$$

$$q_y = G_{cy} \left(\frac{\partial v_c}{\partial z} + \frac{\partial \omega}{\partial y} \right)_{z=\frac{1}{2}t_c} \quad (9)$$

in which t_c = the core thickness; and ω = the lateral deflection of the laminates. In terms of strains, the compatibility equations are written as

$$\frac{\partial \Delta_x}{\partial x} = \varepsilon_{fx} - (\varepsilon_{cx})_{z=\frac{1}{2}t_c} \quad (10)$$

$$\frac{\partial \Delta_y}{\partial y} = \varepsilon_{fy} - (\varepsilon_{cy})_{z=\frac{1}{2}t_c} \quad (11)$$

in which.

ε = normal strain = $\partial u/\partial x$ or $\partial v/\partial y$.

i = x or y direction.

f, c = face and core, respectively.

Δ = interlayer shearing slip = q/K .

K = adhesive stiffness.

In addition to satisfying the force and stress conditions, a solution must also satisfy the geometrical conditions. With respect to the laminates shown in **Figure 7**, the relevant boundary conditions are

$$\sigma_{fx} = 0, \sigma_{cx} = \gamma_y = 0, \text{ and } \omega = 0 \text{ at } x = 0 \text{ and } x = 2a \quad (12)$$

$$\sigma_{fy} = 0, \sigma_{cy} = \gamma_x = 0, \text{ and } \omega = 0 \text{ at } x = 0 \text{ and } x = 2b \quad (13)$$

$$u_c = v_c = 0 \text{ at the middle plane of the laminates, i.e. } z = 0 \quad (14)$$

$$u_f = u_c = 0 \text{ at } x = a \text{ and } v_f = v_c = 0 \text{ at } y = b \text{ in laminates with symmetrical loads} \quad (15)$$

in which $2a$ and $2b$ = the laminates dimensions in x and y directions, respectively; γ_i = the shear strain in the z_i plane, and u_f and v_f = the displacements in the skin along the x and y directions, respectively.

2.4 Equilibrium of the skins

For the laminates in **Figure 7**, the displacement components in the faces are considered as

$$u_f = \sum_{m=1,3,\dots}^{\infty} \sum_{n=1,3,\dots}^{\infty} A_{mn} \cos \alpha_m x \sin \beta_n y \quad (16)$$

$$v_f = \sum_{m=1,3,\dots}^{\infty} \sum_{n=1,3,\dots}^{\infty} B_{mn} \sin \alpha_m x \cos \beta_n y \quad (17)$$

in which $\alpha_m = m \pi/2a$, $\beta_n = n \pi/2b$, and A_{mn} and B_{mn} are unknown coefficients. From Eqs. 16 and 17, expressions for the stresses in the faces can be derived as

$$\sigma_{fx} = \frac{E_f}{\nu^2 - 1} \sum_{m=1,3,\dots}^{\infty} \sum_{n=1,3,\dots}^{\infty} (A_{mn} \alpha_m + \nu B_{mn} \beta_n) \sin \alpha_m x \sin \beta_n y \quad (18)$$

$$\sigma_{fy} = \frac{E_f}{\nu^2 - 1} \sum_{m=1,3,\dots}^{\infty} \sum_{n=1,3,\dots}^{\infty} (B_{mn} \beta_n + \nu A_{mn} \alpha_m) \sin \alpha_m x \sin \beta_n y \quad (19)$$

$$\tau_{xy} = \frac{E_f}{2(1 + \nu)} \sum_{m=1,3,\dots}^{\infty} \sum_{n=1,3,\dots}^{\infty} (A_{mn} \beta_n + B_{mn} \alpha_m) \cos \alpha_m x \cos \beta_n y \quad (20)$$

Expressions for the interlaminar shear stresses q_x and q_y are obtained by differentiating Eqs. 18 to 20 in accordance with the equilibrium Eqs. 1 and 2

$$q_x = \frac{E_f t_f}{1 + \nu} \sum_{m=1,3,\dots}^{\infty} \sum_{n=1,3,\dots}^{\infty} \left(\frac{A_{mn} \alpha_m^2 + \nu B_{mn} \alpha_n \alpha_m}{\nu - 1} - \frac{A_{mn} \beta_n^2 + B_{mn} \alpha_m \beta_n}{2} \right) \cos \alpha_m x \sin \beta_n y \quad (21)$$

$$q_y = \frac{E_f t_f}{1 + \nu} \sum_{m=1,3,\dots}^{\infty} \sum_{n=1,3,\dots}^{\infty} \left(\frac{B_{mn} \beta_n^2 + \nu A_{mn} \alpha_m \beta_n}{\nu - 1} - \frac{B_{mn} \alpha_m^2 + A_{mn} \alpha_m \beta_n}{2} \right) \sin \alpha_m x \cos \beta_n y \quad (22)$$

2.5 Equilibrium of the core

A solution for the core displacement satisfying the equilibrium Eqs. 5 and 6 as well as the boundary conditions in Eqs. 12–15 is taken as

$$u_c = \sum_{m=1,3,\dots}^{\infty} C_m \cos \alpha_m x \sinh \mu_x \alpha_m z \quad (23)$$

$$\vartheta_c = \sum_{m=1,3,\dots}^{\infty} D_n \cos \beta_n y \sinh \mu_y \beta_n z \quad (24)$$

in which $\mu_x = (E_{cx}/G_{cx})^{1/2}$; $\mu_y = (E_{cy}/G_{cy})^{1/2}$; and C_m and D_n are unknown functions of y and x , respectively.

2.6 Serviceability

For the laminates in **Figure 7**, the deflection function which satisfies the boundary conditions in Eq. 12 is given by

$$\omega = \sum_{m=1,3,\dots}^{\infty} W_m \sin \alpha_m x \sin \beta_n y \quad (25)$$

in which W_m = unknown coefficient.

2.7 Interlaminar shear compatibility

The functions C_m and D_n can now be expressed in terms of A_{mn} and B_{mn} by using the compatibility Eqs. 10 and 11. By substituting Eqs. 16, 21, and 23 in Eq. 10 and expression for C_m is obtained as

$$C_m = \sum_{n=1,3,\dots}^{\infty} \frac{1}{\sinh \left(\frac{\mu_x \alpha_m t_c}{2} \right)} \left[\frac{E_f t_f}{K_x (1 + \nu)} \left(\frac{A_{mn} \alpha_m^2 + \nu B_{mn} \beta_n \alpha_m}{1 - \nu} + \frac{A_{mn} \beta_n^2 + B_{mn} \alpha_m \beta_n}{2} \right) + A_{mn} \right] \sin \beta_n y \quad (26)$$

In a similar manner, D_n is obtained from Eqs. 17, 22, 24, and 11 as

$$D_n = \sum_{m=1,3,\dots}^{\infty} \frac{1}{\sinh \left(\frac{\mu_y \beta_n t_c}{2} \right)} \left[\frac{E_f t_f}{K_y (1 + \nu)} \left(\frac{B_{mn} \beta_n^2 + \nu A_{mn} \alpha_m \beta_n}{1 - \nu} + \frac{B_{mn} \alpha_m^2 + A_{mn} \alpha_m \beta_n}{2} \right) + A_{mn} \right] \sin \beta_n y \quad (27)$$

The coefficient B_{mn} can also be expressed in terms of A_{mn} by using the compatibility Eq. 8. By substituting ω , q_x , and u_c in the first equation of Eq. 8, and by equating the coefficients of $\cos \alpha_m x \sin \beta_n y$ in both of its sides, it is found that

$$W_m = \frac{E_f t_f}{G_{cx}(1+\nu)} \left(\frac{A_{mn}\alpha_m + \nu B_{mn}\beta_n}{\nu - 1} - \frac{A_{mn}\beta_n^2 + B_{mn}\alpha_m\beta_n}{2\alpha_m} \right) - \mu_x \coth\left(\frac{\mu_x \alpha_m t_c}{2}\right) \quad (28)$$

$$\times \left[\frac{E_f t_f}{K_x(1+\nu)} \left(\frac{A_{mn}\alpha_m^2 + \nu B_{mn}\beta_n\alpha_m}{1-\nu} + \frac{A_{mn}\beta_n^2 + B_{mn}\alpha_m\beta_n}{2} \right) + A_{mn} \right]$$

In a similar manner, from Eqs. 22, 24, and the second equation in Eq. 9, W_m is found as

$$W_m = \frac{E_f t_f}{G_{cy}(1+\nu)} \left(\frac{B_{mn}\beta_n + \nu A_{mn}\alpha_m}{\nu - 1} - \frac{B_{mn}\alpha_n^2 + A_{mn}\alpha_m\beta_n}{2\beta_n} \right) - \mu_y \coth\left(\frac{\mu_y \beta_n t_c}{2}\right) \quad (29)$$

$$\times \left[\frac{E_f t_f}{K_y(1+\nu)} \left(\frac{B_{mn}\beta_n^2 + \nu B_{mn}\beta_n\alpha_m}{1-\nu} + \frac{B_{mn}\alpha_n^2 + A_{mn}\alpha_m\beta_n}{2} \right) + B_{mn} \right]$$

By equating the right-hand sides of Eqs. 28 and 29, it follows that

$$B_{mn} = \frac{\phi_{mn}}{\psi_{mn}} A_{mn} \quad (30)$$

In which

$$\phi_{mn} = \frac{E_f t_f}{G_{cy}(1+\nu)} \left[-\frac{\alpha_m}{2} + \frac{G_{cy}}{2 G_{cx}} \frac{\beta_n^2}{\alpha_m} + \frac{G_{cy}\mu_y}{2 K_y} \frac{\nu+1}{\nu-1} \alpha_m \beta_n \coth\left(\frac{\mu_y \beta_n t_c}{2}\right) \right. \quad (31)$$

$$+ \frac{G_{cy}\mu_x}{2 K_x} \left(\frac{2\alpha_m^2}{1-\nu} + \beta_n^2 \right) \coth\left(\frac{\mu_x \alpha_m t_c}{2}\right) + \frac{G_{cy}}{G_{cx}} \frac{\alpha_m}{1-\nu} + \frac{\nu \alpha_m}{\nu-1}$$

$$\left. + \mu_x \frac{G_{cy}(\nu+1)}{E_f t_f} \coth\left(\frac{\mu_x \alpha_m t_c}{2}\right) \right]$$

$$\psi_{mn} = \frac{E_f t_f}{G_{cx}(1+\nu)} \left[-\frac{\beta_n}{2} + \frac{G_{cx}}{2 G_{cy}} \frac{\alpha_m^2}{\beta_n} + \frac{G_{cx}\mu_x}{2 K_x} \frac{\nu+1}{\nu-1} \alpha_m \beta_n \coth\left(\frac{\mu_x \alpha_m t_c}{2}\right) \right. \quad (32)$$

$$+ \frac{G_{cx}\mu_y}{2 K_y} \left(\frac{2\beta_n^2}{1-\nu} + \alpha_m^2 \right) \coth\left(\frac{\mu_y \beta_n t_c}{2}\right) + \frac{G_{cx}}{G_{cy}} \frac{\beta_n}{1-\nu} + \frac{\nu \beta_n}{\nu-1}$$

$$\left. + \mu_y \frac{G_{cx}(\nu+1)}{E_f t_f} \coth\left(\frac{\mu_y \beta_n t_c}{2}\right) \right]$$

2.8 Moment equilibrium

The only unknown coefficient now is A_{mn} . This can be determined by using the equilibrium Eq. 7. The moments M_x , M_y , and M_{xy} can be expressed in terms of the stresses components as

$$M_x = \sigma_{fx} t_f h + \int_{-\frac{1}{2}t_f}^{+\frac{1}{2}t_f} \sigma_{cx} z dz \quad (33)$$

$$M_y = \sigma_{fy} t_f h + \int_{-\frac{1}{2}t_f}^{+\frac{1}{2}t_f} \sigma_{cy} z dz \quad (34)$$

$$M_{xy} = -\tau_{xy} t_f h \quad (35)$$

in which $h = t_c + t_f$; $\sigma_{cx} = E_{cx} (\partial u_c / \partial x)$; and $\sigma_{cy} = E_{cy} (\partial v_c / \partial y)$. In terms of these stresses, the equilibrium Eq. 7 becomes

$$t_f h \left(\frac{\partial^2 \sigma_{fx}}{\partial x^2} + 2 \frac{\partial^2 \tau_{xy}}{\partial x \partial y} + \frac{\partial^2 \sigma_{fy}}{\partial y^2} \right) + E_{cx} \frac{\partial^2}{\partial x^2} \int_{-\frac{1}{2}t_f}^{+\frac{1}{2}t_f} \frac{\partial u_c}{\partial x} z dz + E_{cy} \frac{\partial^2}{\partial y^2} \int_{-\frac{1}{2}t_f}^{+\frac{1}{2}t_f} \frac{\partial v_c}{\partial y} z dz = -p \quad (36)$$

Substituting Eqs. 18–20, 23, and 24 in Eq. 35 yields the following expression for A_{mn}

$$A_{mn} = \frac{P_{mn}}{\xi_{mn}} \quad (37)$$

in which P_{mn} = Fourier series expansion of the applied load, p .

$$\begin{aligned} \xi_{mn} = & \frac{E_f t_f h}{\nu^2 - 1} \left(\alpha_m^3 + \nu \beta_n \alpha_m^2 \frac{\phi_{mn}}{\psi_{mn}} \right) - \frac{E_f t_f h}{1 + \nu} \left(\alpha_m \beta_n^2 + \beta_n \alpha_m^2 \frac{\phi_{mn}}{\psi_{mn}} \right) \\ & + \frac{E_f t_f h}{\nu^2 - 1} \left(\nu \alpha_m \beta_n^2 + \beta_n^3 \frac{\phi_{mn}}{\psi_{mn}} \right) \\ & + \frac{2 E_{cx} \mu_y C'_{mn}}{\mu_x^2} \left(\frac{\mu_x \alpha_m t_c}{2} \cosh \left(\frac{\mu_x \alpha_m t_c}{2} \right) - \sinh \left(\frac{\mu_x \alpha_m t_c}{2} \right) \right) \\ & + \frac{2 E_{cy} \beta_n D'_{mn}}{\mu_y^2} \left(\frac{\mu_y \beta_n t_c}{2} \cosh \left(\frac{\mu_y \beta_n t_c}{2} \right) - \sinh \left(\frac{\mu_y \beta_n t_c}{2} \right) \right) \end{aligned} \quad (38)$$

in which

$$C'_{mn} = \frac{1}{\sinh \left(\frac{\mu_x \alpha_m t_c}{2} \right)} \left[\frac{E_f t_f}{K_x (1 + \nu)} \left(\frac{\alpha_m^2 + \nu \beta_n \alpha_m \frac{\phi_{mn}}{\psi_{mn}}}{\nu - 1} - \frac{\beta_n^2 + \beta_n \alpha_m \frac{\phi_{mn}}{\psi_{mn}}}{2} \right) - 1 \right] \quad (39)$$

$$D'_{mn} = \frac{1}{\sinh \left(\frac{\mu_y \beta_n t_c}{2} \right)} \left[\frac{E_f t_f}{K_y (1 + \nu)} \left(\frac{\nu \beta_n \alpha_m + \beta_n^2 \frac{\phi_{mn}}{\psi_{mn}}}{\nu - 1} - \frac{\beta_n \alpha_m + \alpha_m^2 \frac{\phi_{mn}}{\psi_{mn}}}{2} \right) - \frac{\phi_{mn}}{\psi_{mn}} \right] \quad (40)$$

In the particular case where $G_{cx} = G_{cy} = G_c$; $E_{cx} = E_{cy} = E_c$; and $K_x = K_y = K$, hence $\mu_x = \mu_y = (E_c/G_c)^{1/2} = \mu$, thus the expressions for ϕ_{mn} , ψ_{mn} , and ξ_{mn} become

$$\begin{aligned} \xi_{mn} = & \frac{E_f t_f h}{G_c (1 + \nu)} \left[\frac{\alpha_m}{2} + \frac{\beta_n^2}{2 \alpha_m} + \frac{G_c \mu \beta_n \alpha_m \nu + 1}{2 K \nu - 1} \coth \left(\frac{\mu \beta_n t_c}{2} \right) \right. \\ & \left. + \frac{G_c \mu}{2 K} \left(\frac{2 \alpha_m^2}{1 - \nu} + \beta_n^2 \right) \coth \left(\frac{\mu \alpha_m t_c}{2} \right) + \frac{G_c \mu (1 + \nu)}{E_f t_f} \coth \left(\frac{\mu \alpha_m t_c}{2} \right) \right] \end{aligned} \quad (41)$$

$$\begin{aligned} \psi_{mn} = & \frac{E_f t_f}{G_c (1 + \nu)} \left[\frac{\beta_n}{2} + \frac{\alpha_m^2}{2 \beta_n} + \frac{G_c \mu \beta_n \alpha_m \nu + 1}{2 K \nu - 1} \coth \left(\frac{\mu \alpha_m t_c}{2} \right) \right. \\ & \left. + \frac{G_c \mu}{2 K} \left(\frac{2 \beta_n^2}{1 - \nu} + \alpha_m^2 \right) \coth \left(\frac{\mu \beta_n t_c}{2} \right) + \frac{G_c \mu (1 + \nu)}{E_f t_f} \coth \left(\frac{\mu \beta_n t_c}{2} \right) \right] \end{aligned} \quad (42)$$

$$\begin{aligned} \xi_{mn} = & \frac{E_f t_f h}{\nu^2 - 1} \left(\alpha_m^3 + \nu \beta_n \alpha_m^2 \frac{\phi_{mn}}{\psi_{mn}} \right) - \frac{E_f t_f h}{\nu + 1} \left(\alpha_m \beta_n^2 + \beta_n \alpha_m^2 \frac{\phi_{mn}}{\psi_{mn}} \right) \\ & + \frac{E_f t_f h}{\nu^2 - 1} \left(\nu \alpha_m \beta_n^2 + \beta_n^3 \frac{\phi_{mn}}{\psi_{mn}} \right) \\ & + 2 G_c \alpha_m C'_m \left(\frac{\mu \alpha_m t_c}{2} \cosh \left(\frac{\mu \alpha_m t_c}{2} \right) - \sinh \left(\frac{\mu \alpha_m t_c}{2} \right) \right) \\ & + 2 G_c \beta_n D'_n \left(\frac{\mu \beta_n t_c}{2} \cosh \left(\frac{\mu \beta_n t_c}{2} \right) - \sinh \left(\frac{\mu \beta_n t_c}{2} \right) \right) \end{aligned} \quad (43)$$

in which

$$C'_{mn} = \frac{1}{\sinh\left(\frac{\mu \alpha_m t_c}{2}\right)} \left[\frac{E_f t_f}{K(1+\nu)} \left(\frac{\alpha_m^2 + \nu \beta_n \alpha_m \frac{\phi_{mn}}{\psi_{mn}}}{\nu - 1} - \frac{\beta_n^2 + \beta_n \alpha_m \frac{\phi_{mn}}{\psi_{mn}}}{2} \right) - 1 \right] \quad (44)$$

$$D'_{mn} = \frac{1}{\sinh\left(\frac{\mu \beta_n t_c}{2}\right)} \left[\frac{E_f t_f}{K(1+\nu)} \left(\frac{\nu \beta_n \alpha_m + \beta_n^2 \frac{\phi_{mn}}{\psi_{mn}}}{\nu - 1} - \frac{\beta_n \alpha_m + \alpha_m^2 \frac{\phi_{mn}}{\psi_{mn}}}{2} \right) - \frac{\phi_{mn}}{\psi_{mn}} \right] \quad (45)$$

By following the above analytical formulation and considering the in-plane load shown in **Figure 9**, the following solution is obtained

$$\begin{aligned} \sigma_{fx} = & \sum_{m=1,3,..}^{\infty} \sum_{n=1,3,..}^{\infty} [A_{mn} \lambda'_{z1} + C_{mn} \lambda'_{z2}] S_x S_y \\ & + \left(\sigma_{xo} + \sigma_{cxo} \frac{t_c}{t_f} \right) \sum_{m=1}^{\infty} \sum_{n=1}^{\infty} \frac{2}{a \alpha_m} \frac{2}{b \beta_n} S_x S_y \end{aligned} \quad (46)$$

$$\begin{aligned} \sigma_{fy} = & \sum_{m=1,3,..}^{\infty} \sum_{n=1,3,..}^{\infty} [A_{mn} \lambda'_{z3} + C_{mn} \lambda'_{z4}] S_x S_y \\ & + \left(\sigma_{yo} + \sigma_{cyo} \frac{t_c}{t_f} \right) \sum_{m=1}^{\infty} \sum_{n=1}^{\infty} \frac{2}{a \alpha_m} \frac{2}{b \beta_n} S_x S_y \end{aligned} \quad (47)$$

$$\begin{aligned} \tau_{fxy} = & \sum_{m=1,3,..}^{\infty} \sum_{n=1,3,..}^{\infty} A_{mn} \left[\frac{G_{fxy}}{E_{cx}} \phi_x \Big|_{z=t_c} \left(-\frac{\beta_n}{\alpha_m} + \nu_{cxy} \frac{\alpha_m}{\beta_n} \right) + \frac{G_{fxy} \beta_n}{K_x} \lambda_{gn1} + \frac{G_{fxy} \beta_n}{K_y} \lambda_{gk2} \right] C_x C_y \\ & + \sum_{m=1,3,..}^{\infty} \sum_{n=1,3,..}^{\infty} C_{mn} \left[\frac{G_{fxy}}{E_{cy}} \phi_y \Big|_{z=t_c} \left(-\frac{\alpha_m}{\beta_n} + \nu_{cxy} \frac{\beta_n}{\alpha_m} \right) + \frac{G_{fxy} \beta_n}{K_x} \lambda_{gn2} + \frac{G_{fxy} \alpha_m}{K_y} \lambda_{gk1} \right] C_x C_y \end{aligned} \quad (48)$$

$$q_x = \sum_{m=1,3,..}^{\infty} \sum_{n=1,3,..}^{\infty} (A_{mn} \lambda_{gn1} + C_{mn} \lambda_{gn2}) C_x S_y \quad (49)$$

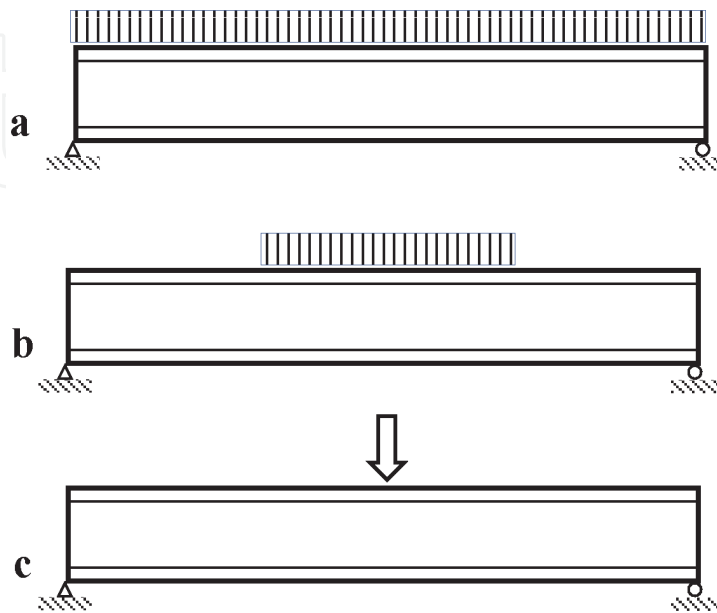


Figure 9. Three loading cases used for verification, (a) uniform load, (b) central uniform load, (c) central concentrated load.

$$\mathbf{q}_y = \sum_{m=1,3,\dots}^{\infty} \sum_{n=1,3,\dots}^{\infty} (C_{mn}\lambda_{gk1} + A_{mn}\lambda_{gk2}) S_x C_y \quad (50)$$

$$\begin{aligned} \tau_{cxz} = & \sum_{m=1,3,\dots}^{\infty} \sum_{n=1,3,\dots}^{\infty} \int_{z=0}^z \phi_x dz A_{mn} \left[-\alpha_m + \frac{G_{cxy}}{E_{cx}} \beta_n \left(-\frac{\beta_n}{\alpha_m} + \nu_{cxy} \frac{\alpha_m}{\beta_n} \right) \right] C_x S_y \\ & + \frac{G_{cxy}}{E_{cy}} \sum_{m=1,3,\dots}^{\infty} \sum_{n=1,3,\dots}^{\infty} \int_{z=0}^z \phi_y dz C_{mn} \beta_n \left(-\frac{\alpha_m}{\beta_n} + \nu_{cxy} \frac{\beta_n}{\alpha_m} \right) C_x S_y \end{aligned} \quad (51)$$

$$\begin{aligned} \tau_{cyz} = & \sum_{m=1,3,\dots}^{\infty} \sum_{n=1,3,\dots}^{\infty} \int_{z=0}^z \phi_y dz C_{mn} \left[-\beta_n + \frac{G_{cxy}}{E_{cy}} \alpha_m \left(-\frac{\alpha_m}{\beta_n} + \nu_{cxy} \frac{\beta_n}{\alpha_m} \right) \right] C_y S_x \\ & + \frac{G_{cxy}}{E_{cx}} \sum_{m=1,3,\dots}^{\infty} \sum_{n=1,3,\dots}^{\infty} \int_{z=0}^z \phi_x dz A_{mn} \alpha_m \left(-\frac{\beta_n}{\alpha_m} + \nu_{cxy} \frac{\alpha_m}{\beta_n} \right) S_x C_y \end{aligned} \quad (52)$$

in which

$$A_{mn} = \frac{\frac{\lambda_{y3}}{\lambda_{y2}} - \frac{\lambda_{y6}}{\lambda_{y5}}}{\frac{\lambda_{y1}}{\lambda_{y2}} - \frac{\lambda_{y4}}{\lambda_{y5}}} \quad (53)$$

$$C_{mn} = \frac{\frac{\lambda_{y3}}{\lambda_{y1}} - \frac{\lambda_{y6}}{\lambda_{y4}}}{\frac{\lambda_{y2}}{\lambda_{y1}} - \frac{\lambda_{y5}}{\lambda_{y4}}} \quad (54)$$

$$\begin{aligned} \lambda_{y1} &= \frac{\lambda'_{z1}}{E_{fx}} - \frac{\nu_{fxy}\lambda'_{z3}}{E_{fy}} - \frac{\phi_x|_{z=t_c}}{E_{cx}} + \frac{\alpha_m\lambda_{gn1}}{K_x} \\ \lambda_{y2} &= \frac{\lambda'_{z2}}{E_{fx}} - \frac{\nu_{fxy}\lambda'_{z4}}{E_{fy}} + \frac{\nu_{cxy}\phi_y|_{z=t_c}}{E_{cy}} + \frac{\alpha_m\lambda_{gn2}}{K_x} \\ \lambda_{y3} &= \frac{2}{a\alpha_m} \frac{2}{b\beta_n} \left[\frac{\sigma_{xo} + \sigma_{cxo} \frac{t_c}{t_f}}{E_{fx}} - \nu_{fxy} \frac{\sigma_{yo} + \sigma_{cyo} \frac{t_c}{t_f}}{E_{fy}} + \frac{\sigma_{cxo}}{E_{cx}} + \nu_{cxy} \frac{\sigma_{cyo}}{E_{cy}} \right] \\ \lambda_{y5} &= \frac{\lambda'_{z4}}{E_{fy}} - \frac{\nu_{fyx}\lambda'_{z2}}{E_{fx}} - \frac{\phi_y|_{z=t_c}}{E_{cy}} + \frac{\beta_n\lambda_{gk1}}{K_y} \\ \lambda_{y6} &= \frac{2}{a\alpha_m} \frac{2}{b\beta_n} \left[\frac{\sigma_{yo} + \sigma_{cyo} \frac{t_c}{t_f}}{E_{fy}} - \nu_{fyx} \frac{\sigma_{xo} + \sigma_{cxo} \frac{t_c}{t_f}}{E_{fx}} + \frac{\sigma_{cyo}}{E_{cy}} + \nu_{cyx} \frac{\sigma_{cxo}}{E_{cx}} \right] \end{aligned}$$

2.9 Effects of bonding stiffness on the performance of laminates

The complexity of the closed-form solution makes it difficult to ascertain manually the effects of non-rigid bonding on the laminates' responses. Thus, we developed windows-based toolkits to evaluate the obtained complex mathematical formulas [19, 24]. For verification, consider the laminates shown in **Figure 10**. The skins and core properties are: $t_f = 0.04$ in. ($1 \text{ e-}3$ m), $E_f = 10^7$ psi ($6.9 \text{ e}10$ Pa), $t_c = 2.0$ in. ($5 \text{ e-}2$ m), $E_c = 2 \times 10^4$ psi (110 kPa), and $G_c = 10^4$ psi (69 MPa). Three loading types are considered as shown in **Figure 10**. The laminated panel is under three loading cases.

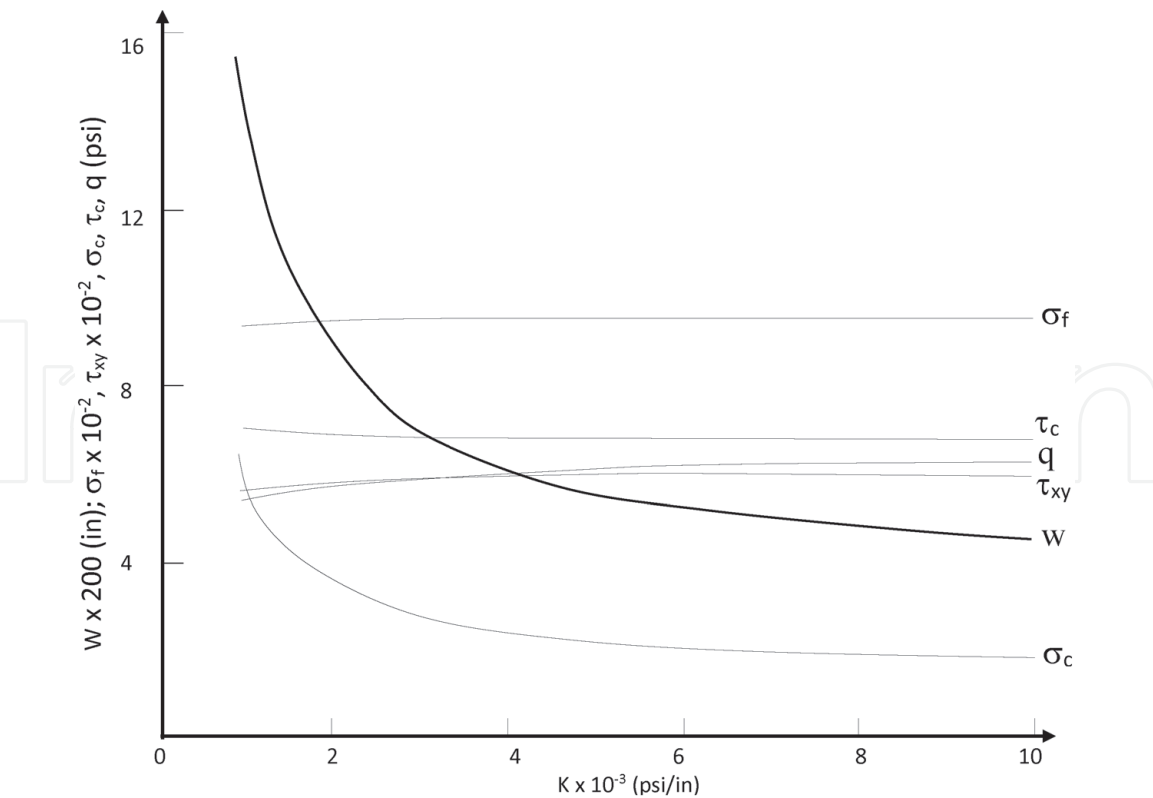


Figure 10.
Bonding effects on deflection and stresses (load case a).

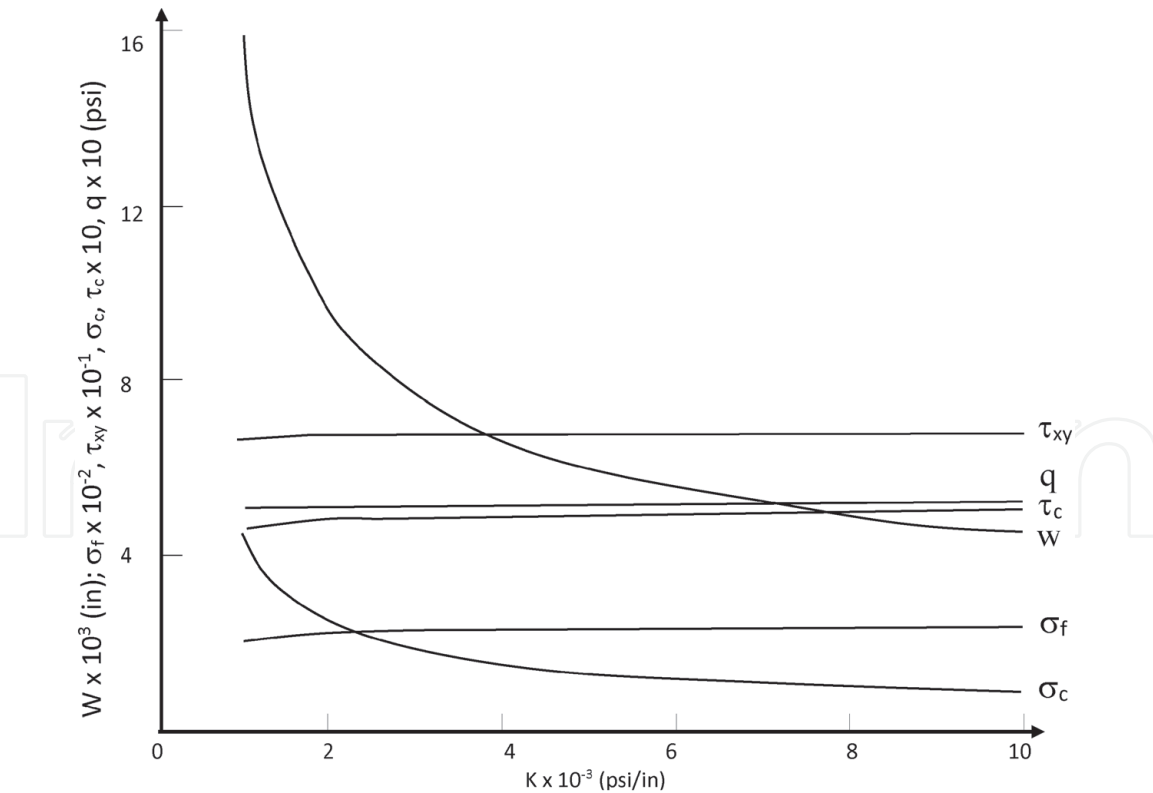


Figure 11.
Bonding effects on deflection and stresses (load case b).

Figures 11–15 show the maximum normal and shear stress, and the deflection obtained for each load. The figures show that the bonding stiffness, K , has significant effect on the deflection in its low range, beyond which the effect is unnoticeable thus the literature common assumption of perfect rigid bonding may

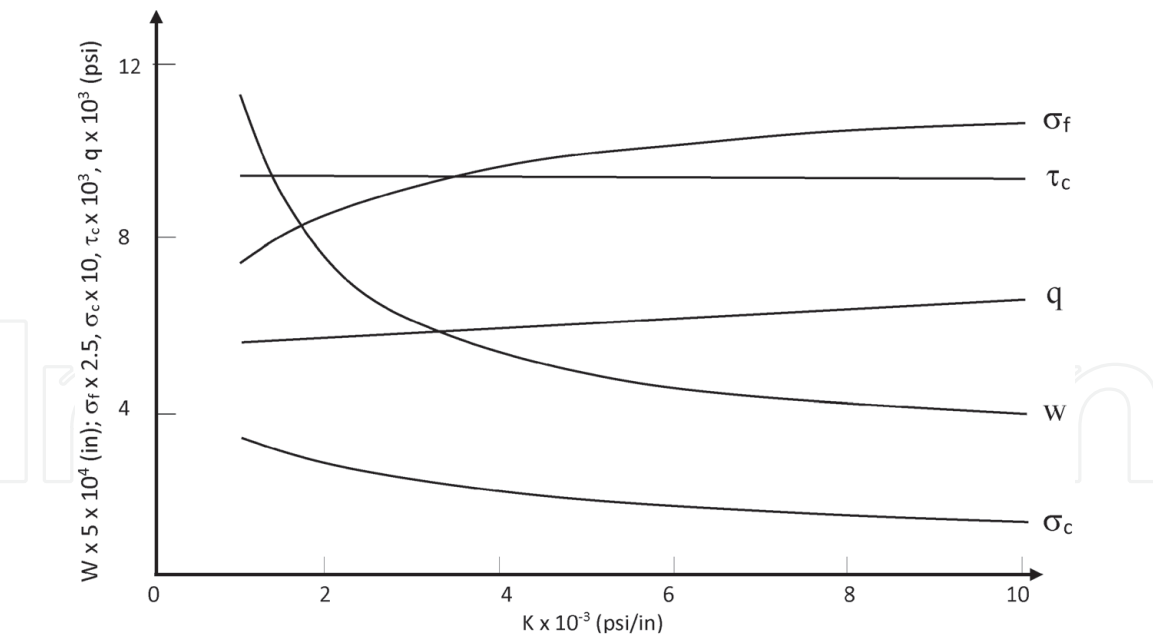


Figure 12.
Bonding effects on deflection and stresses (load case c).

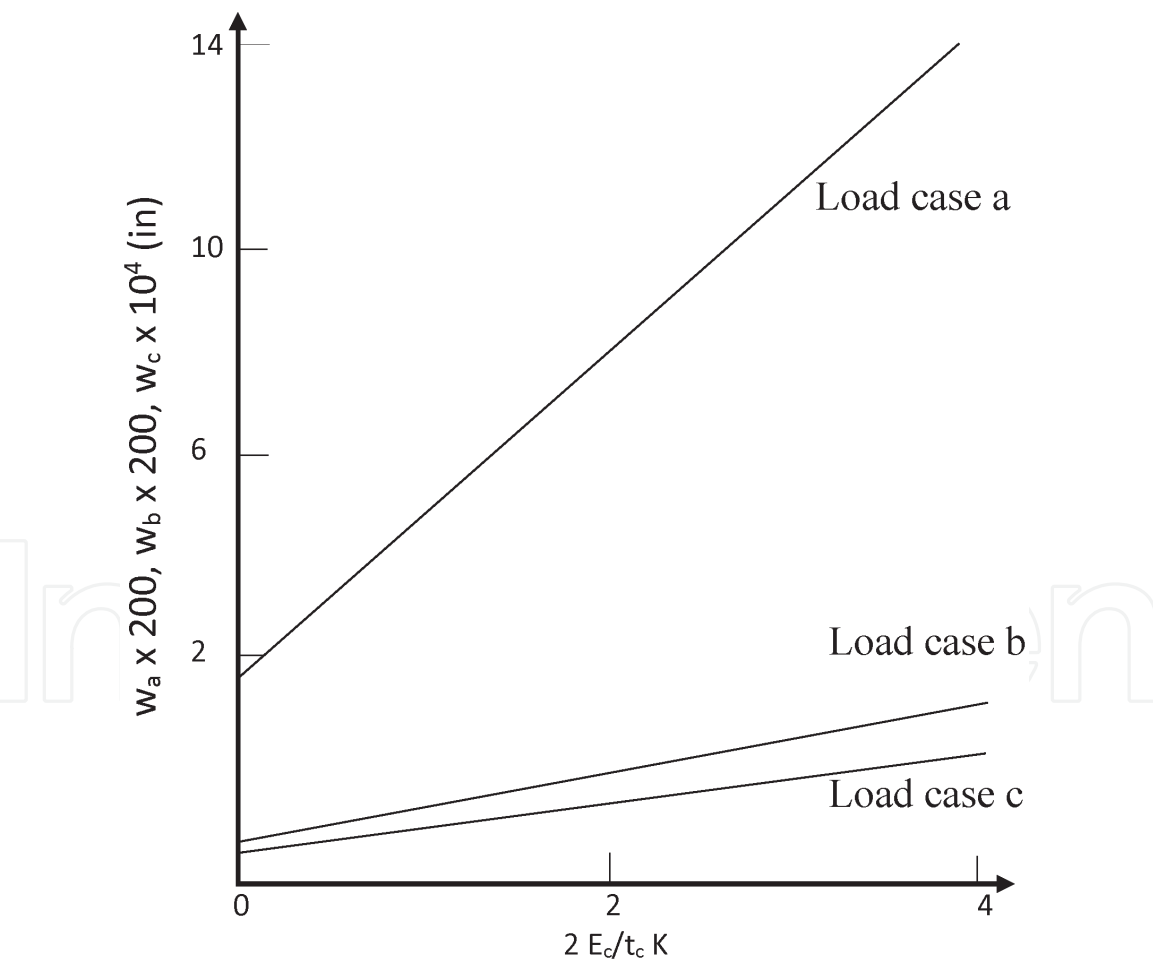


Figure 13.
Effect of $(2 E_c / t_c K)$ on maximum deflection.

apply. To elaborate, the deflection of the panel under uniform load has increased 14 orders of magnitude when the K values changed from 3,000–2,000 psi/in. ($8 \text{ e}8$ – $5.4 \text{ e}8$ Pa/m) to 10–9 ksi/in. (2.7 – 2.4 GPa/m). Furthermore, the K value showed

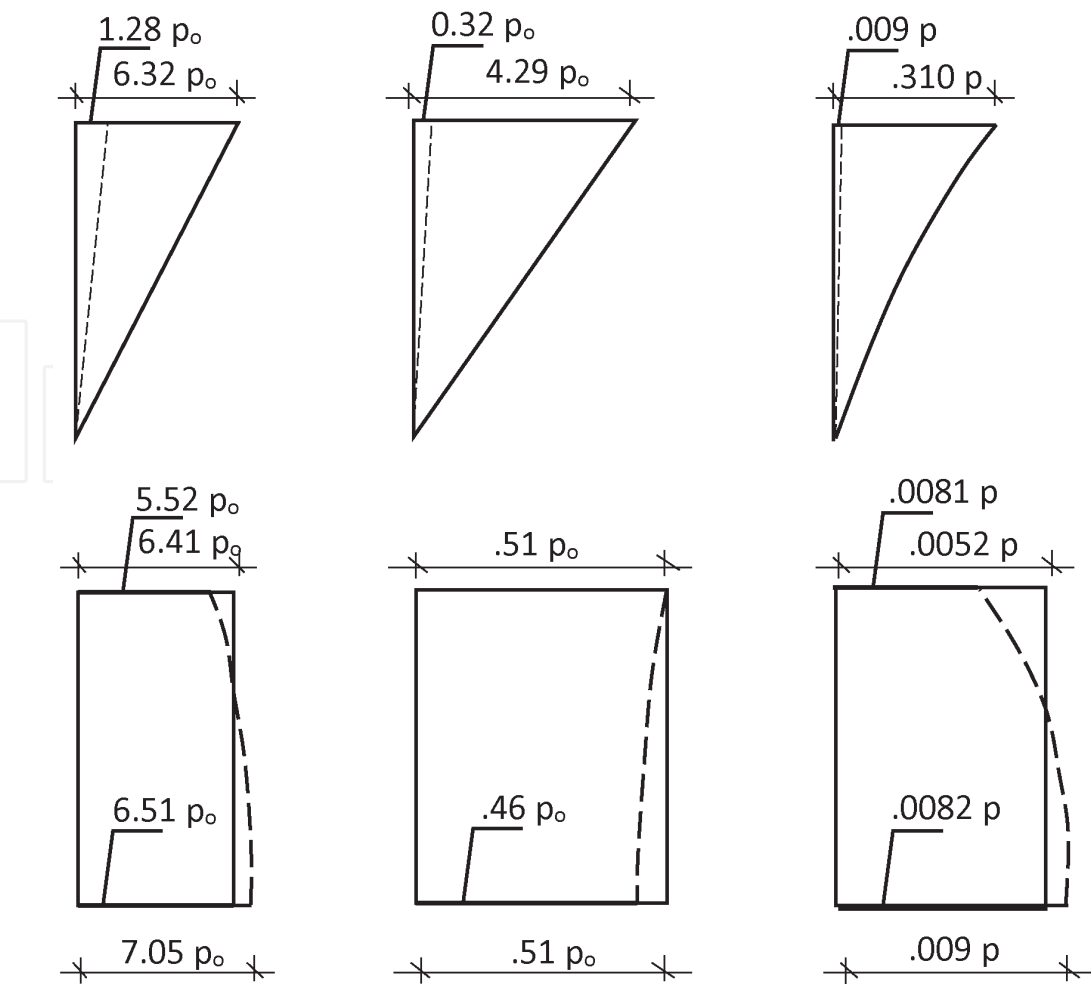


Figure 14.
Bonding effects on stress distributions in Core.

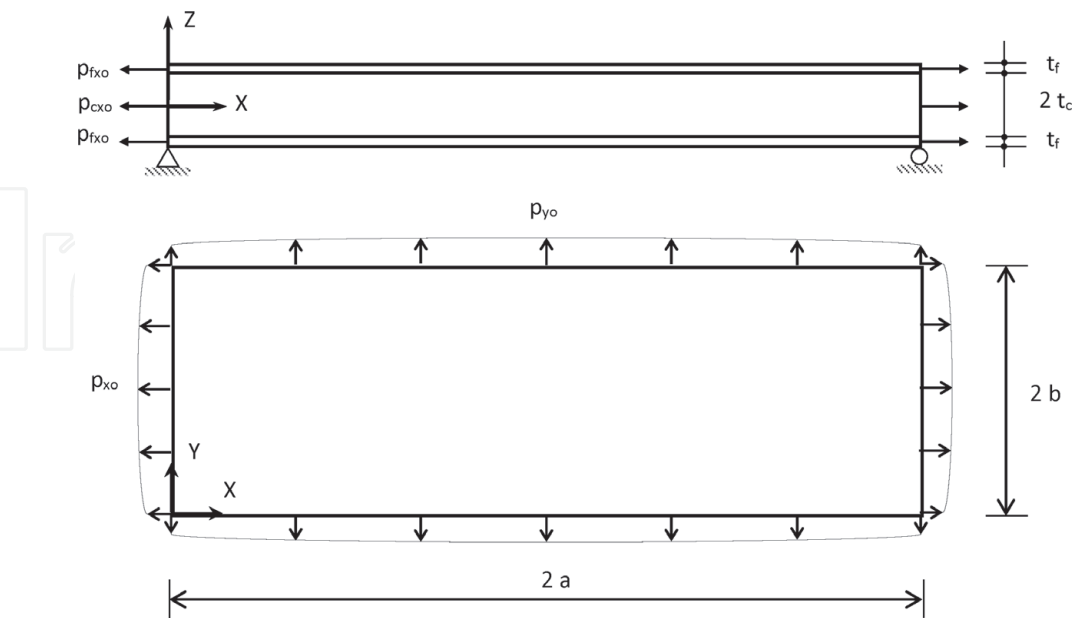


Figure 15.
A laminate under In-plane loads.

insignificant effect on the interlayer shear stress and reduced slightly the core normal stress. The later reduction is compensated by an increase in the skin stress. This discovery is expected because the higher the K value the less deflection, thus less deformation in the thick layer, i.e., the core.

By using the existing rigid-bonding based solutions from the literature [13, 15], normal and shear stresses in the skins, and the transverses shear stress in the core may be determined with an acceptable margin of error. Nonetheless, the bonding stiffness should be included in the analysis whenever the deflection is the quantity of interest. This is an important point. To illustrate this important finding, consider the laminates in **Figure 10**. For a bonding stiffness of 4 ksi/in. (1.0 GPa/m), the deflection and stresses in the laminates are obtained with the present theory as $\omega = 0.0313$ in. (8×10^{-4} m); $\sigma_f = 950$ psi (6.6×10^6 Pa); $\tau_{xy} = 592$ psi (4×10^6 Pa); and $\tau_c = 6.7$ psi (46 kPa). The corresponding values as obtained using rigid bonding are $\omega = 0.0168$ in. (4×10^{-4} m); $\sigma_f = 939$ psi (6.5×10^6 Pa); $\tau_{xy} = 610$ psi (4.2×10^6 Pa); and $\tau_c = 6.6$ psi (4.5 kPa). Comparison of these two sets of results indicates that the deflection determined by the existing theory is underestimated by 46% whereas the stresses of the two are comparable. There is another takeaway from this solution. This study has yet to bring up another important discovery. From an economic perspective, a rigid, i.e., expensive, adhesive would be unnecessary for the manufacturing of the panels if the core is made of soft material such as foam. The converse would be unwise. Because the core and bonding together contribute to the integrity and overall performance of the laminates, the ratio of core-to-bonding stiffness is introduced, and its effect is shown in **Figure 14**. The figure agrees with this discovery.

Laminated panels in building construction undergo various types of loads. The previous section presented a model for panels under flexural loads. In-plane loads are very common in walls and gable roof applications. The analytical formulation for this type of panels is similar to the previously presented one for flexural loads. Thus, it will be summarized in the following section to highlight the differences between the two formulations. The laminate shown in **Figures 9** and **16** is subjected

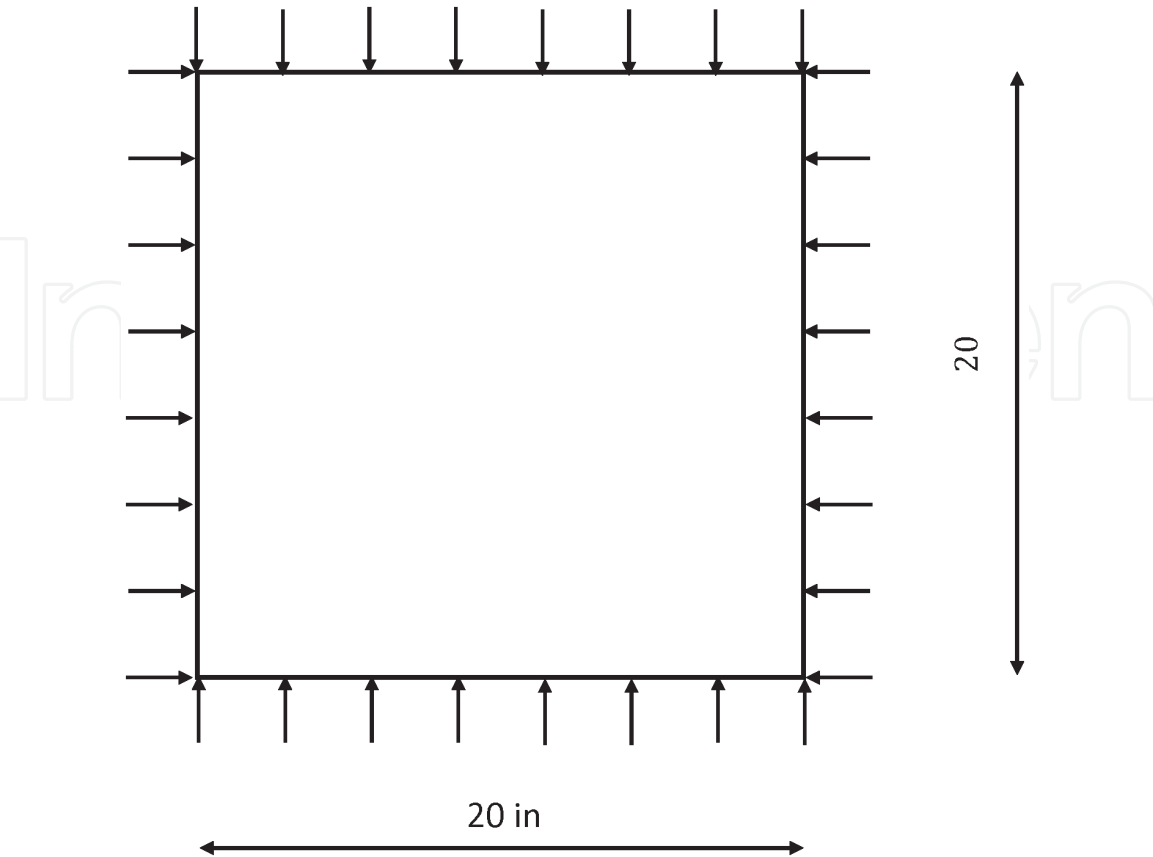


Figure 16.
A plane view of a panel under biaxial edge load.



Figure 17.
A biaxial edge load applied to faces.



Figure 18.
A biaxial edge load applied to Core.



Figure 19.
A biaxial edge load applied to faces and Core.

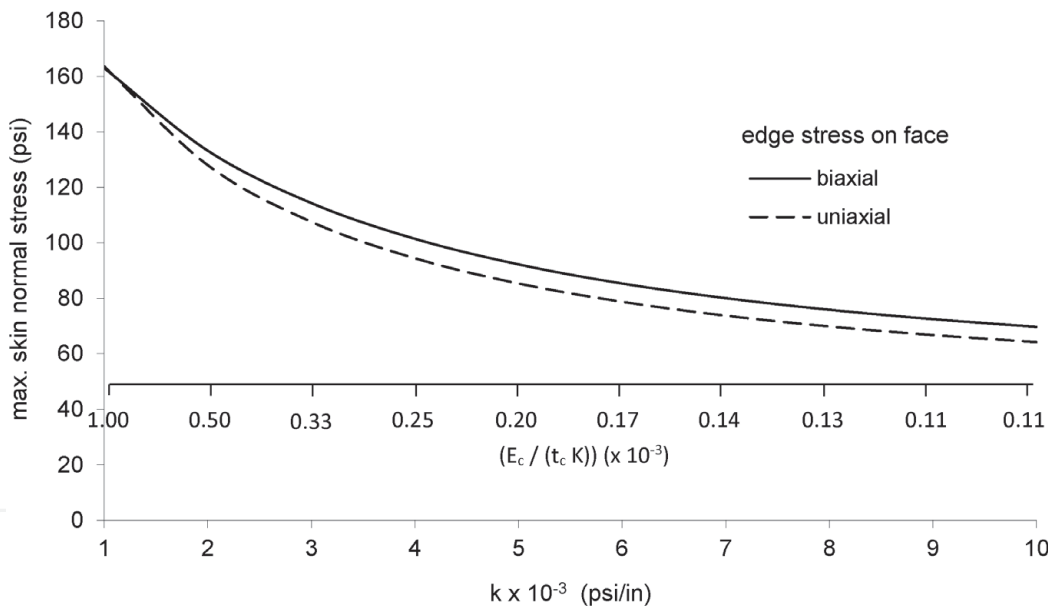


Figure 20.
Effects of bond stiffness on face Normal stress due to face edge load.

to uniform in-plane loadings: a biaxial stress $\sigma_{fxo} = \sigma_{fyo} = 208.3 \text{ psi}$ (1.4 MPa), and a uniaxial stress $\sigma_{fxo} = 208.3 \text{ psi}$ (1.4 MPa). **Figures 17** and **18** show the skin and core loading, whereas **Figure 19** shows the superimposed loading. A wide range of isotropic adhesive stiffness was used, varying from ksi/in (0.25GPa/m) to 10 ksi/in (2.5 GPa/m). This range covers non-rigid to rigid stiffnesses. The normal stress in the faces at the panel center and the shear stress in the faces at the panel corner are shown graphically in **Figures 20–25**.

As under bending loads, the figures, the bonding stiffness affects the response of the laminates. For example, the face normal stress, σ_f , is greatly affected by the K

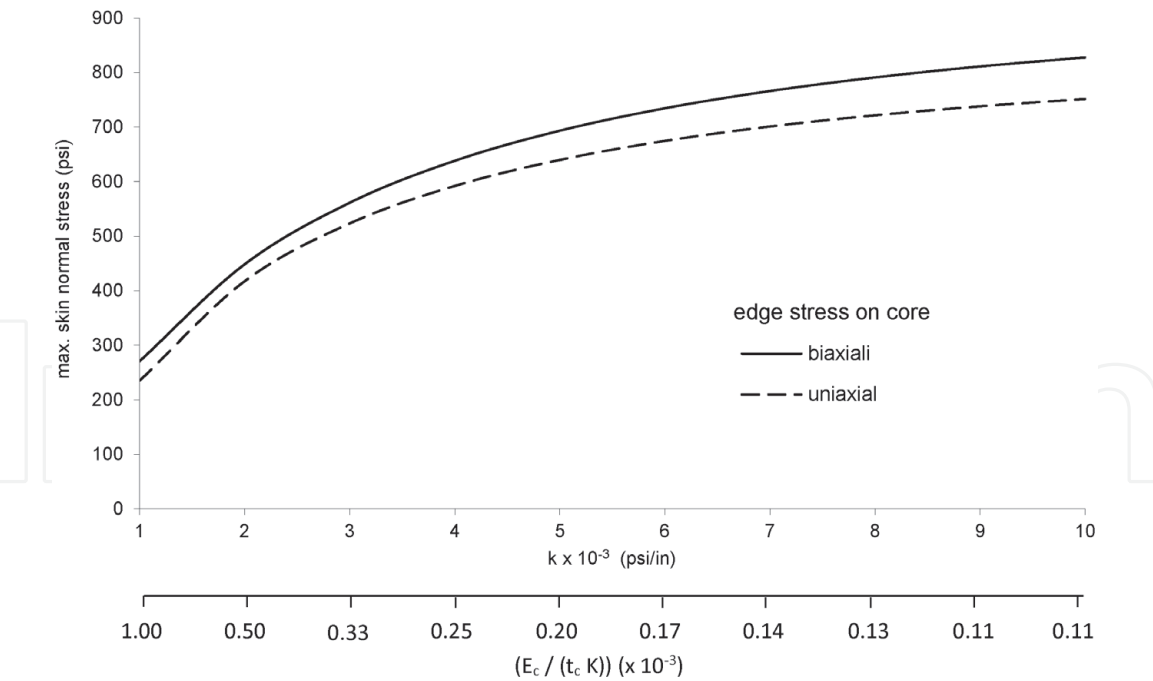


Figure 21.
Effects of bond stiffness on face Normal stress due to Core edge load.

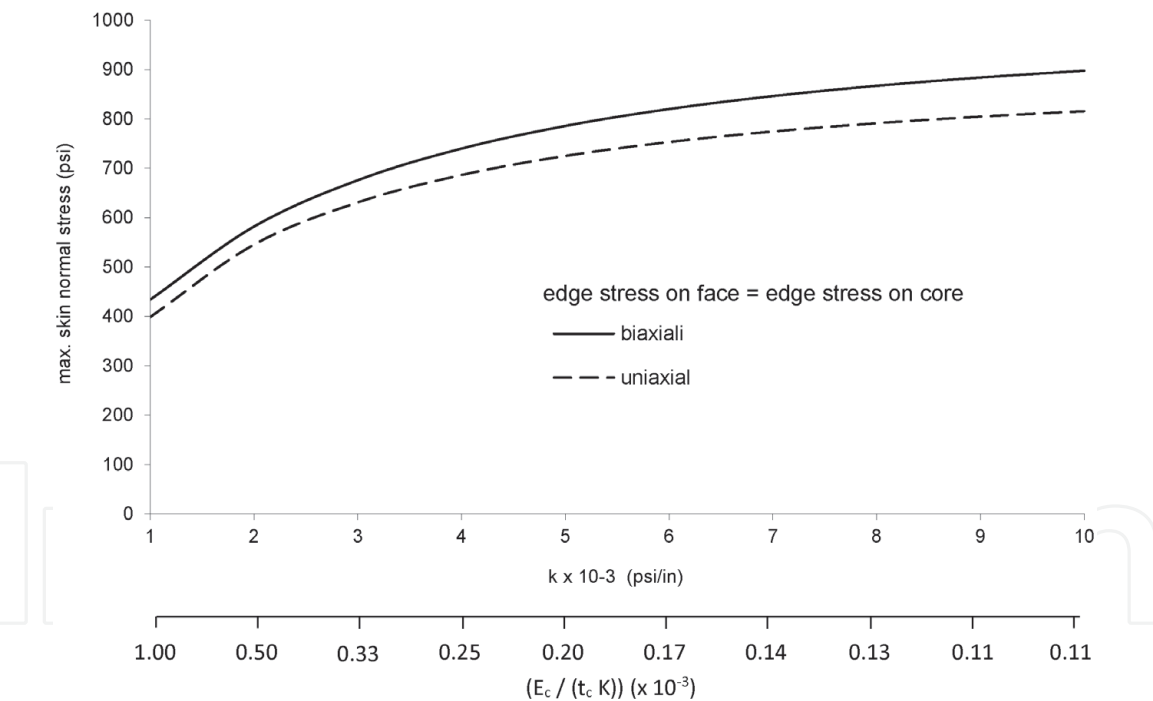


Figure 22.
Effects of bond stiffness on face Normal stress due to face and Core edge load.

value in its lower range; but beyond a certain level of stiffness (which varies from panel to panel), the bonding layer can be practically considered as rigid. A change in K-value for example from 1 to 2 ksi/in (0.25–0.50 GPa/m) induces a stress decrease almost 6 times in the uniaxial case and 5 times in the biaxial case greater than when K changes from 9–10 ksi/in. (2.25–2.50 GPa/m). The changes are 24% and 27% due to uniaxial core and combined edge loads, respectively, 32% and 22% due to biaxial core and combined edge loads, respectively. In all in-load cases, the face and interlayer shear stresses are not affected significantly by the bonding stiffness.

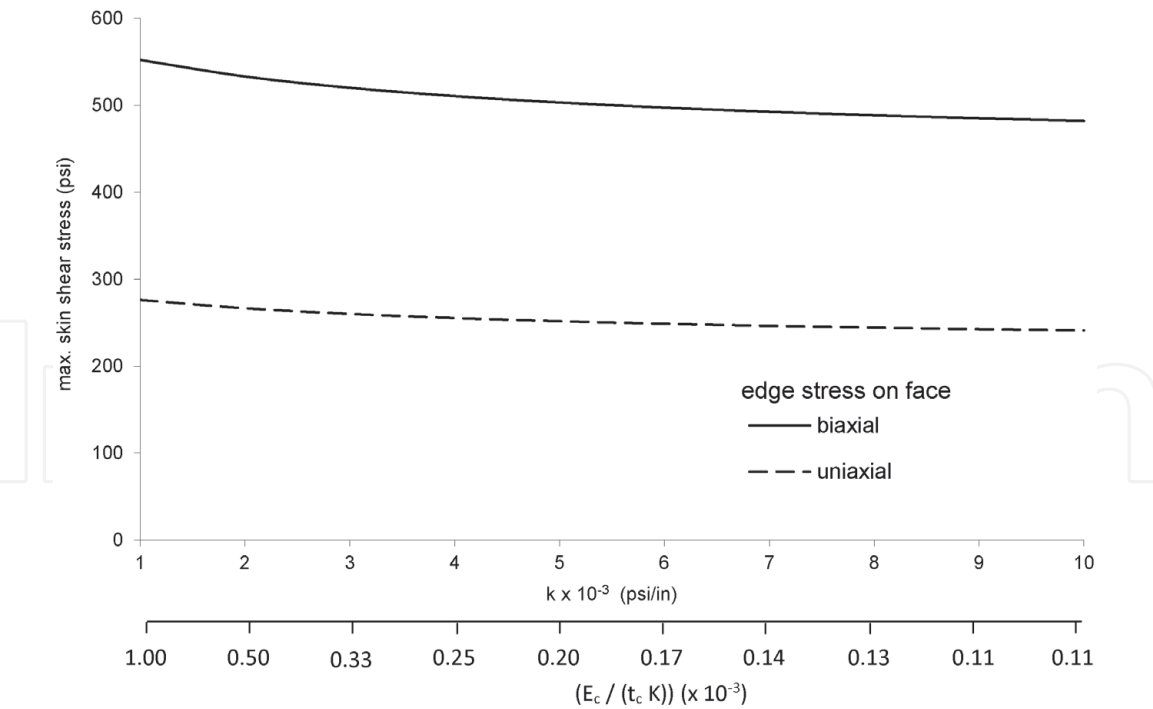


Figure 23.
Effects of bond stiffness on face shear stress due to face edge load.

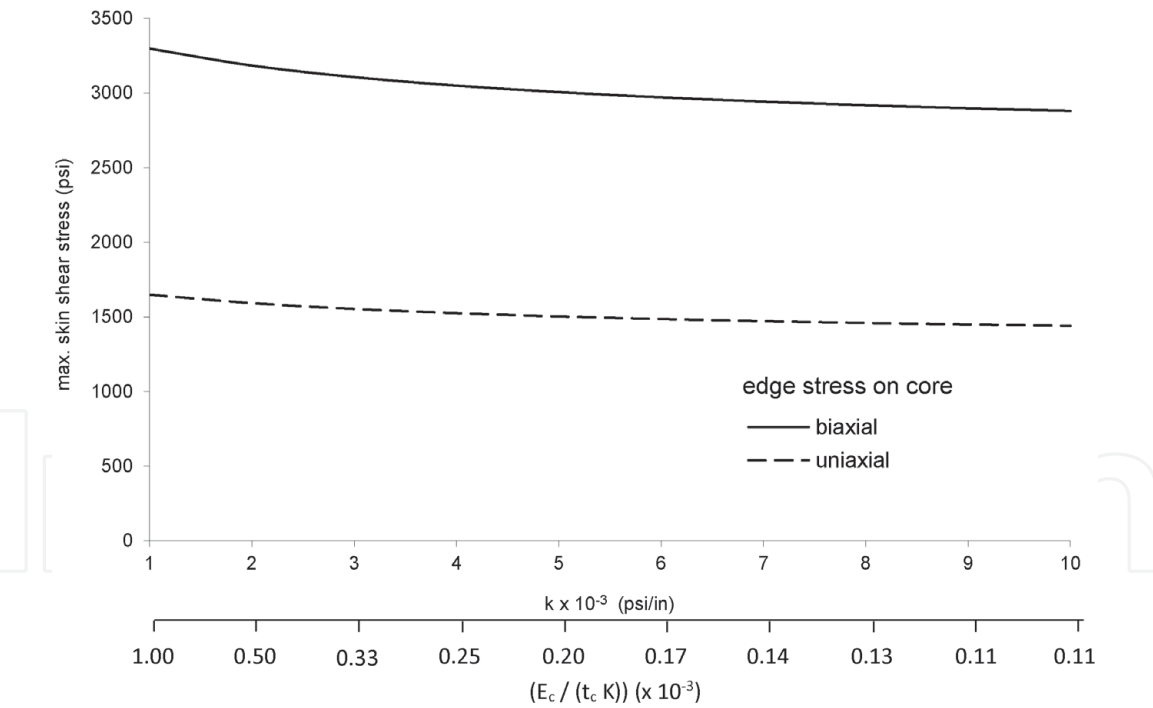


Figure 24.
Effects of bond stiffness on face shear stress due to Core edge load.

The absence of transverse loads yields no transverse shear which coexists with in-plane shear.

As found in panels under flexural loads, a panel made of adhesive with high stiffness and soft cores is uneconomic, and the converse is unsafe. Thus, the applications of the theories that assumed perfectly rigid bonding should produce acceptable performance results if the bonding stiffness is high and the core material is compatible with the adhesive.

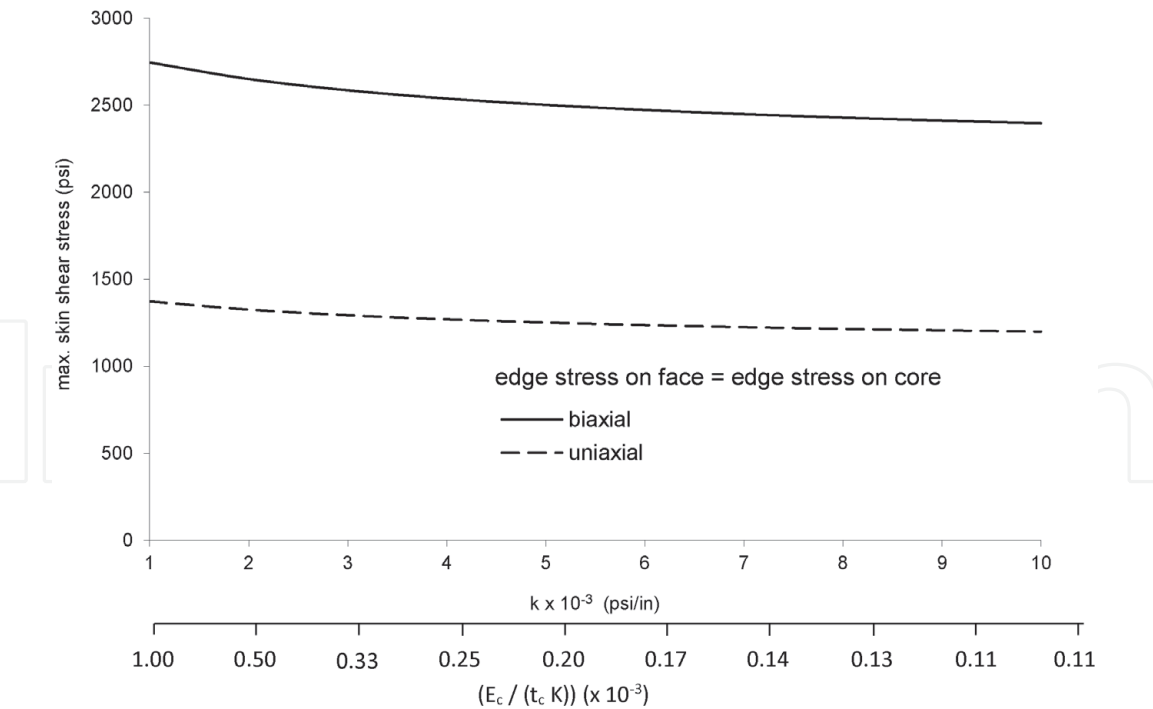


Figure 25.
Effects of bond stiffness on face shear stress due to Core edge load.

3. Engineered gussett plates in IN timber systems

3.1 Introduction

Metal gusset plates are used in timber light frame construction since 1955 to create structural joints. The concept of perforated gussets joins the timber members without the use of nails, screws, or glue. The building construction industry is familiar with the timber framing that use that concept, thus is empowered to meet myriad of challenges including complex blueprints and structural joints [18]. However, the incorporated laterally unsupported areas in the gussets are subject to out-of-plane deformation due to excessive forces. Currently, the literature incorporates some experimental data for the metal connectors [1, 13, 18], and empirical design recommendations [13, 20]. To our knowledge, the out-of-plane deformation of the gussets was not engineered so far. This chapter introduces for the first-time relevant design aids to fill the relevant voids in the existing literature [1, 13, 16, 20]. To provide a well-balanced presentation, we presented the analytical background of the problem at hands, upon which a design procedure was established and introduced.

3.2 Framework analysis

Any structural analysis requires material and geometrical properties of the members that constitute the framing system. The constitutive relations of timber are well established and applied since the appearance of Hooke's law in 1676. In this study, we considered timber as a 3D orthotropic material for which the required mechanical properties are adopted from Ref. 25. The gusset-timber in-plane and out of plane interactions are complex to simulate [1, 13, 20]. This study idealized the in-plane and out of plane interactions using spring elements. For this purpose, the stiffness matrix is

$$[K] = \begin{bmatrix} K_{11} & K_{12} \\ \text{symm} & K_{11} \end{bmatrix}$$

where K_{ii} is a 6x6 diagonal sub-matrix with the axial and shear constants, whereas K_{ij} is zero matrix.

Because of the inherited complexity of the problem at hands, the finite element method is deemed a direct and simple method to harness all the previously described component developed for our approach. **Figures 26–28** show FE models that represent various timber joints. The material properties for timber and gusset are: $E_{\text{gusset}} = 30 \text{ ksi}$, $E_{\text{l-timber}} = 1.6 \text{ ksi}$, $E_{\text{t-timber}} = 0.08 \text{ ksi}$, $E_{\text{r-timber}} = 0.108 \text{ ksi}$,

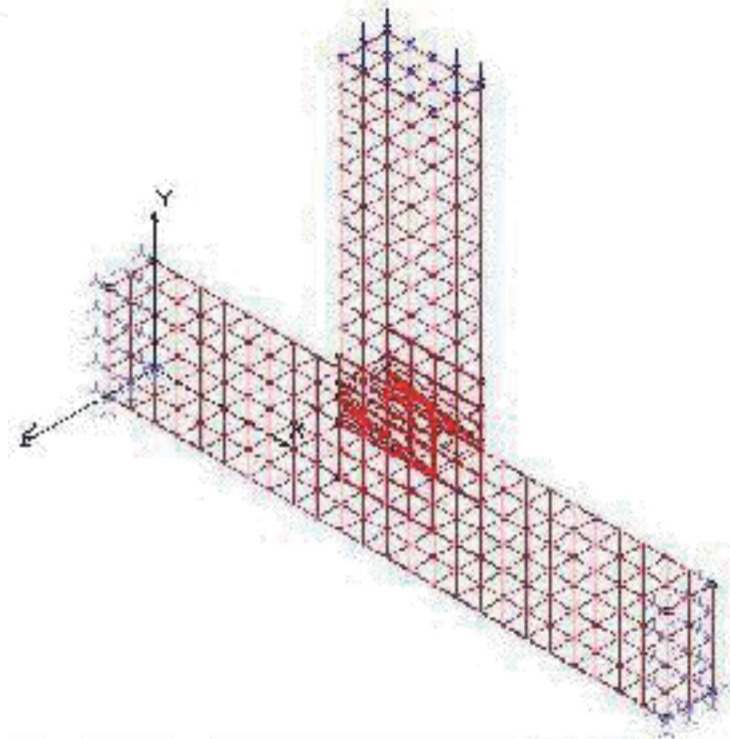


Figure 26.
A screen view of the framework analysis - a.

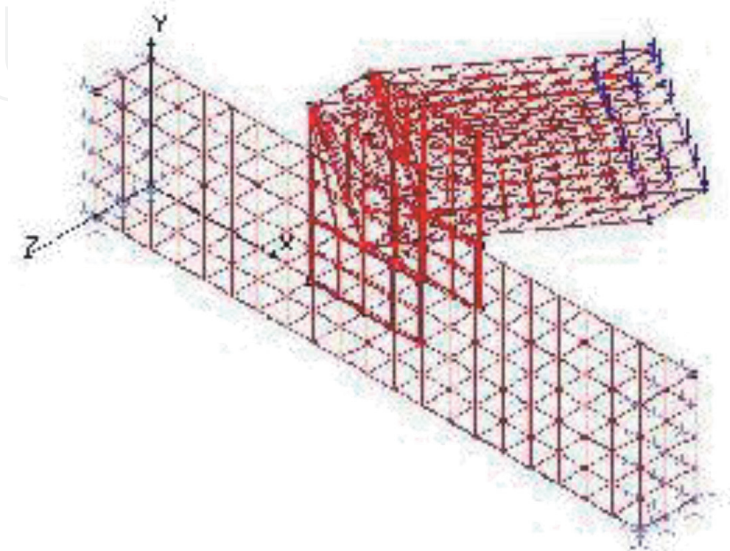


Figure 27.
A screen view of the framework analysis - b.

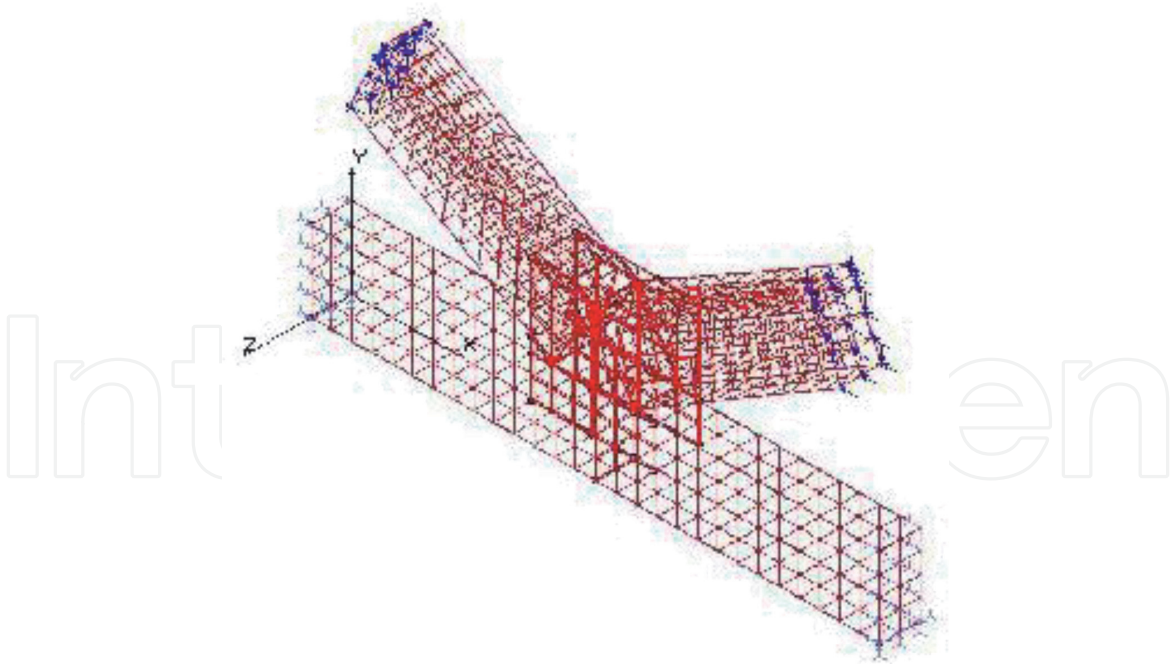


Figure 28.
A screen view of the framework analysis - c.

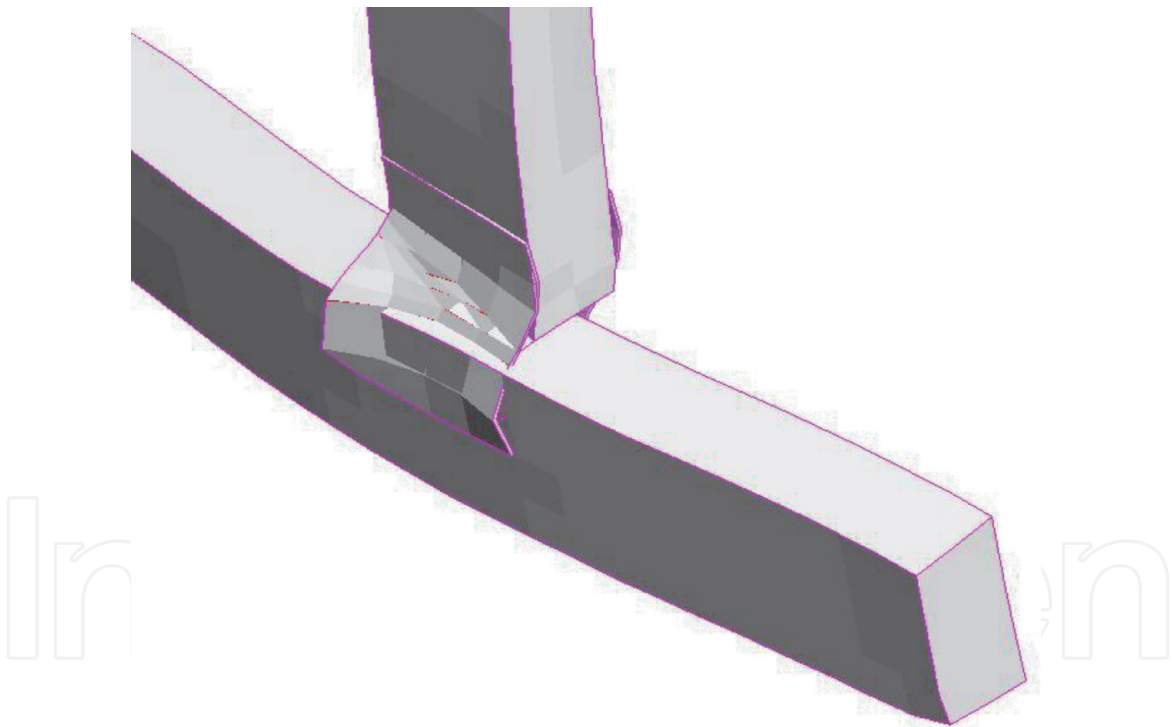


Figure 29.
Out of plane deformation of the gusset in Figure 26.

$G_{lr} = 0.102$ ksi, $G_{lt} = 0.124$ ksi, $G_{rt} = 0.111$ ksi, $\nu_{lr} = 0.29$, $\nu_{lt} = 0.45$, $\nu_{rt} = 0.39$, $\nu_{tr} = 0.37$, $\nu_{rl} = 0.04$, $\nu_{tl} = 0.03$, where E is modulus of elasticity, n is Poisson's ratio; l , t and r stand for longitudinal, tangential and radial directions, respectively. **Figures 29–31** show the corresponding deformed shapes. As shown in the figures, the gusset plates undergo bending and withdrawal deformations.

Figure 32 shows the performance of the gusset in **Figure 26**. The figure shows 80% and 70% drops in the critical load (the load at which out of plane deformations occur) under compression and shear, respectively. Under chord and gap shears, the critical load decreases and increases by 70% and 27%, respectively. This finding

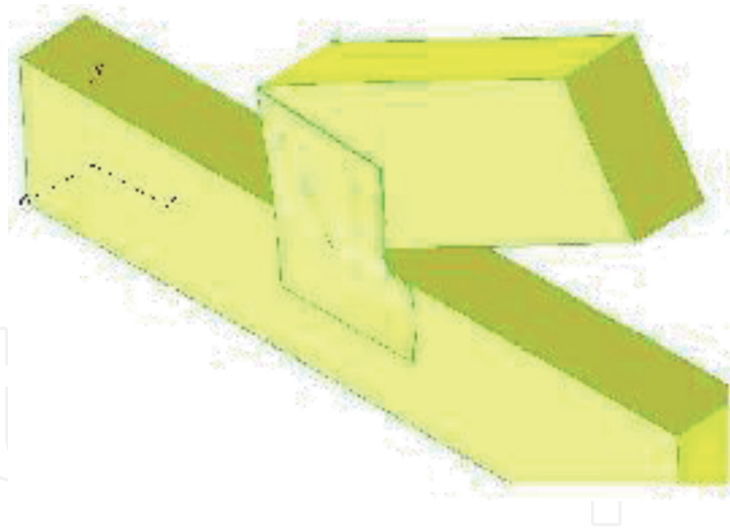


Figure 30.
Out of plane deformation of the gusset in Figure 27.

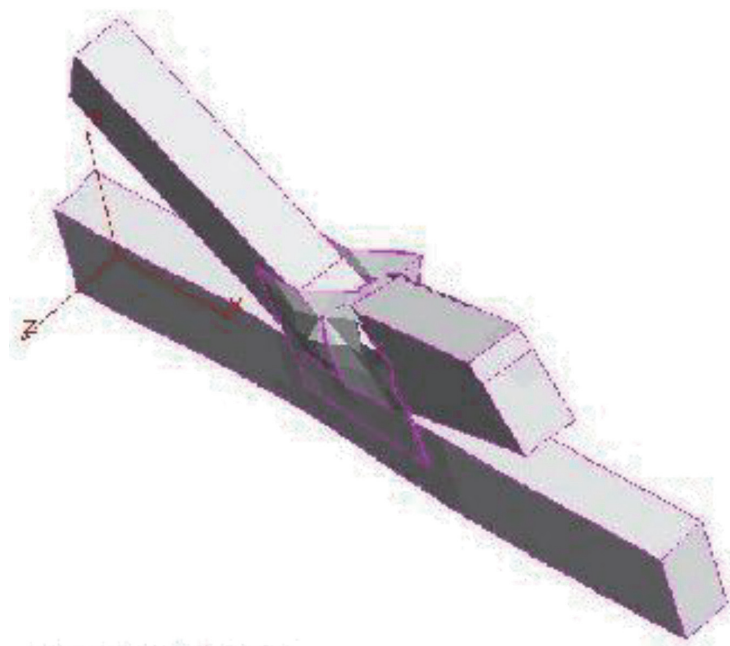


Figure 31.
Out of plane deformation of the gusset in Figure 28.

suggests that the plate is weaker under than compression for areas smaller than 2.0 in² and the converse is true for larger areas. For practical applications, the smaller ratio of gap/shear length the higher the critical load. For example, the load increases by 50% when the ratio is $\frac{3}{4}$ rather than $\frac{4}{3}$. For all applications, the smaller the gusset unsupported area or its thickness the higher the critical values, and this agrees with conventional theories [17]. One of the takeaways from this analysis is that chord and web shears rather than compression [13] are the key drivers for the gusset instability. In addition, an answer the question of what constitutes effective gusset area can now be answered. An area of 1.0 in² would be conservative regardless of thicknesses whereas caution is advised when using an area larger than 2.0 in². However, designers can use large areas in combination with thicker plates. In general, the design needs not to depend on one variable only, gap, or chord length, or gusset area. This is another takeaway. To validate our analytic approach, we used the data obtained by the truss plate institute from testing various connections made of Southern Pine. **Figure 33** compares both results. The figure shows close agreement between the critical values.

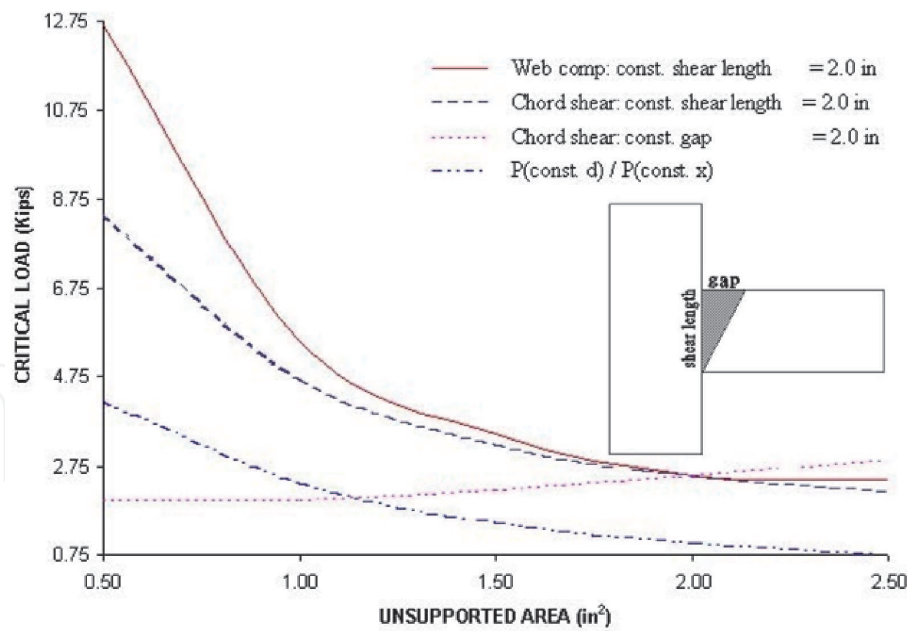


Figure 32.
Effects of gap and shear length the plate in Figure 26.

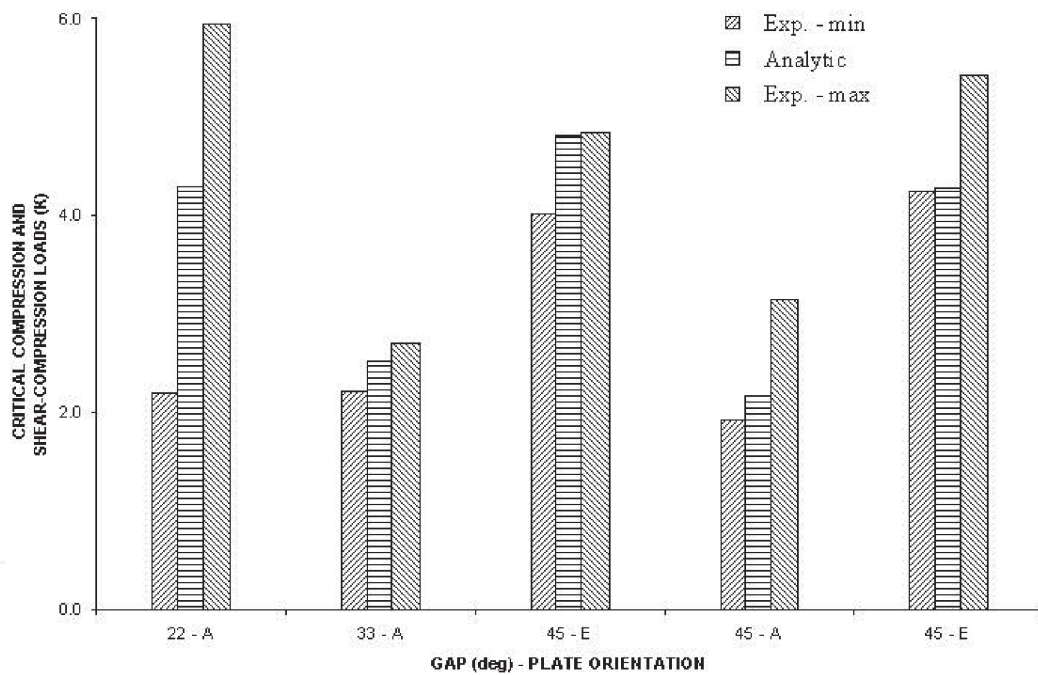


Figure 33.
Comparison of experimental critical loads for the gusset in Figure 26.

Based on the confidence established in the analytic formulation, we then moved on to gusset plates with three laterally unsupported areas. **Figures 34–36** show the deformations obtained for areas A, B, and C. It should be noted that these figures show the gusset plate only. In addition, the web force compresses area A and shears areas B and C.

Figure 37 shows that area B deforms before A under chord shears. This occurs only under web compressions for areas up to about 1.5 in², afterwards this sequence reverses. When area B is between 0.5 in² and 1.0 in², the critical load decreases by 54% and 36% under compressions and shears, respectively. When the area is between 1.0 in² and 2.0 in², the decrease is 28% under compression and 26% under shear. These findings are not accustomed in practice where only web compressions

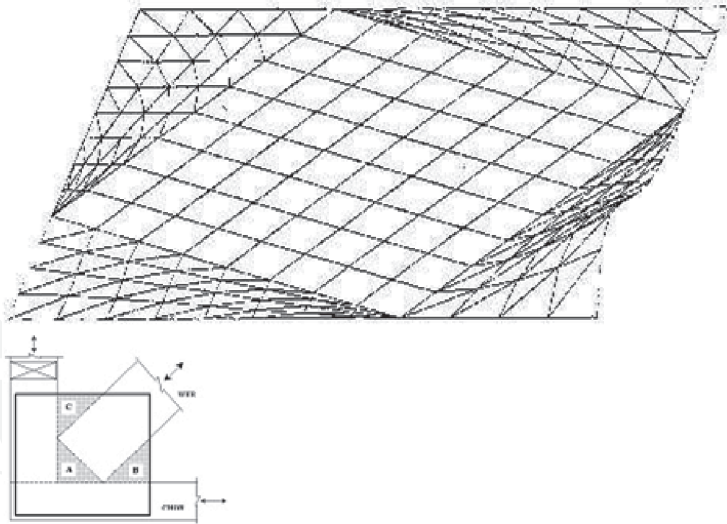


Figure 34.
Deformation of area a in the joint in Figure 34.

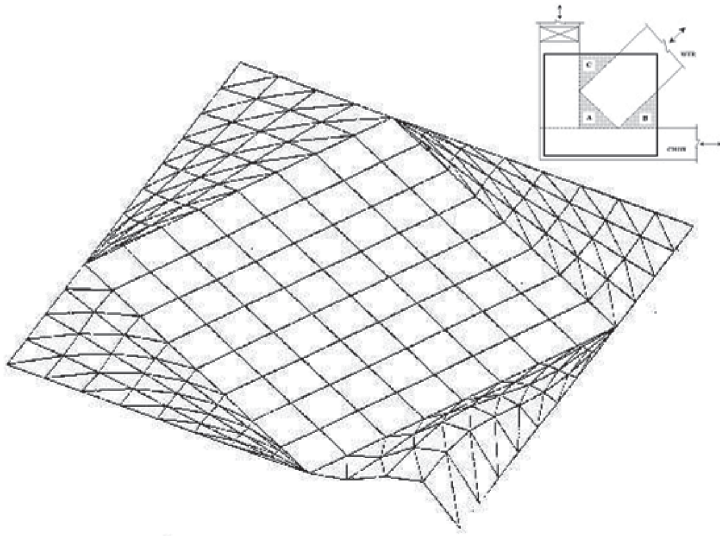


Figure 35.
Deformation of area B in the joint in Figure 34.

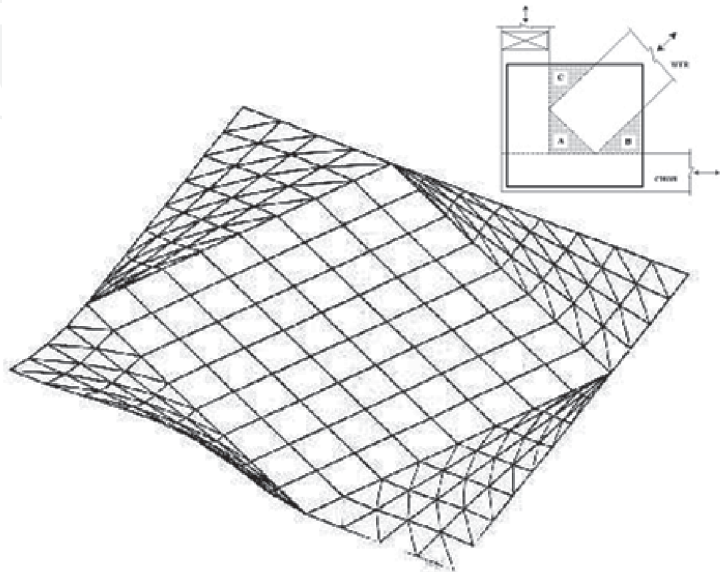


Figure 36.
Deformation of area C in the joint in Figure 34.

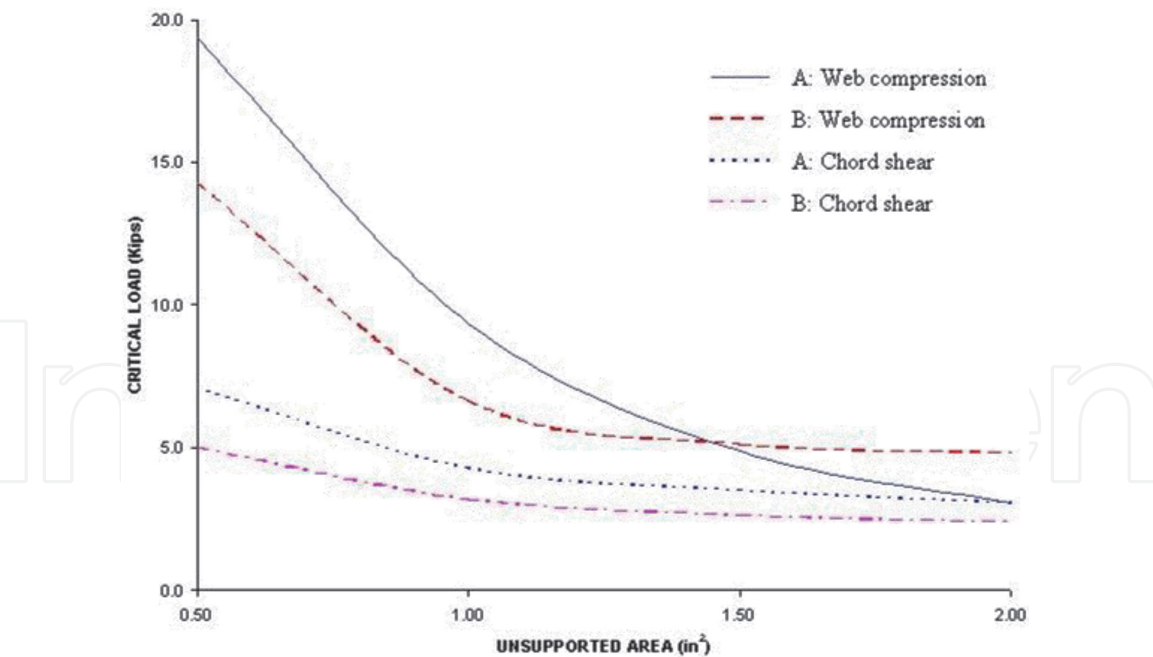


Figure 37.
Effects of unsupported areas on shears and web compressions (0.030 in).

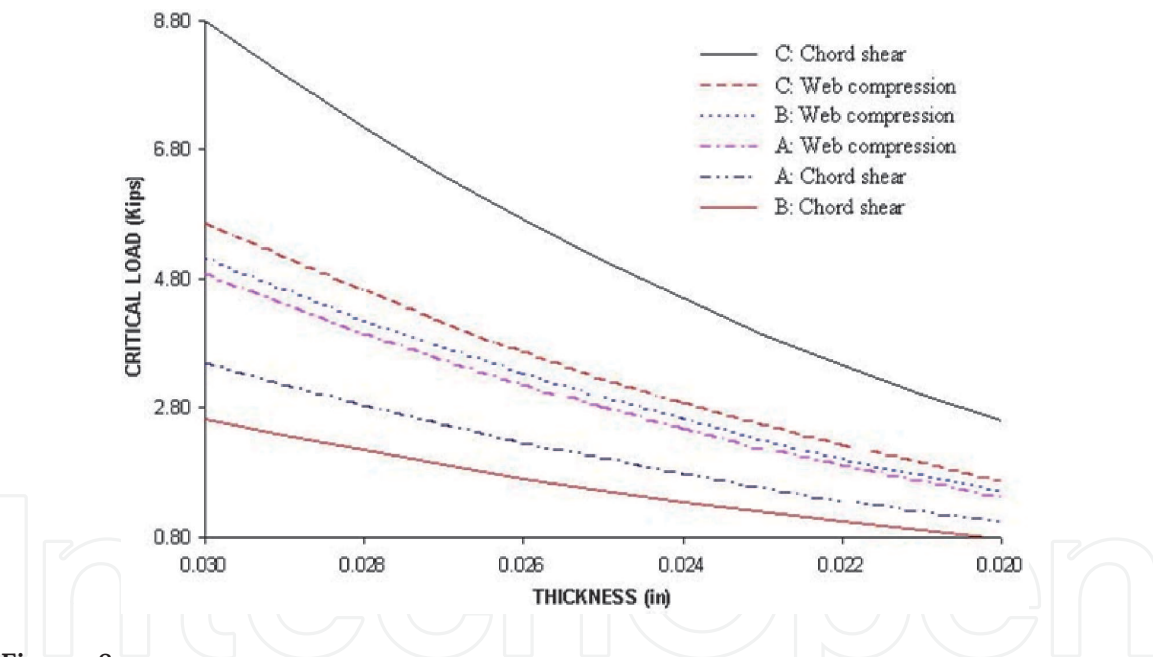


Figure 38.
Comparison between web compression and chord shear critical loads of areas a, B and C (1.5 in²).

is the driving factor for deformation. **Figures 37 and 38** affirms that the chord shear has more effects on the deformation of the gusset than compression. In agreement with the analysis conducted for single area and fundamentals of engineering mechanics, the smaller the gusset or the larger its thickness, the larger the critical values.

3.3 Design aids for gusset plates

To bring the outcomes of our investigation to everyday practice, **Figures 39–42** show design curves. To use any of the figures, area A or B is first located on the horizontal axis, then a vertical line is drawn to intersect with the curve with the

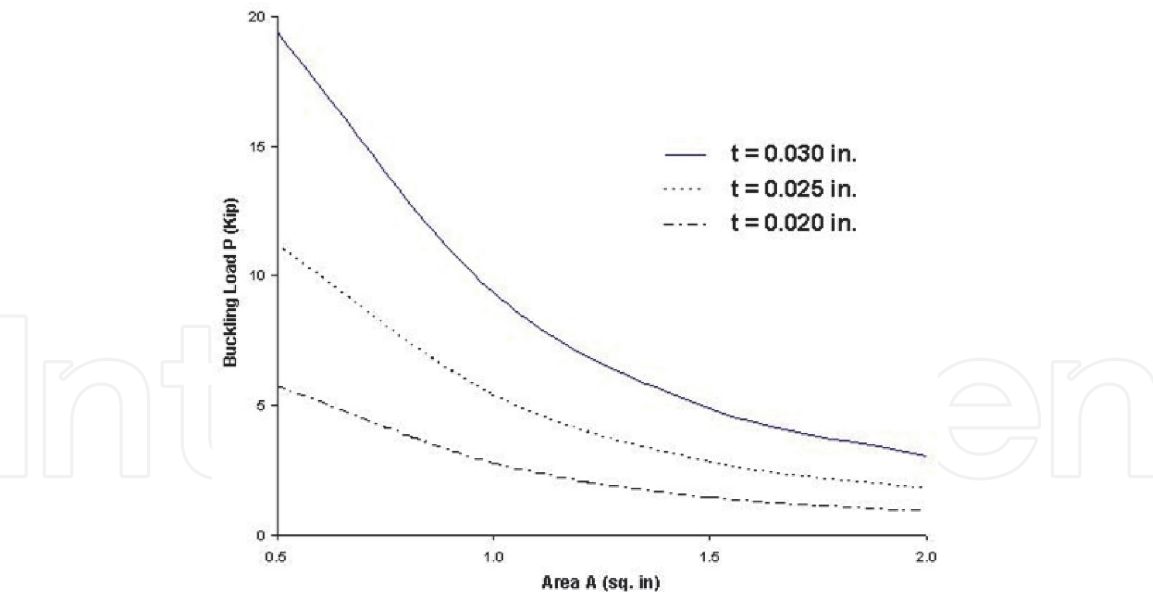


Figure 39.
Design critical loads for gusset under web compression.

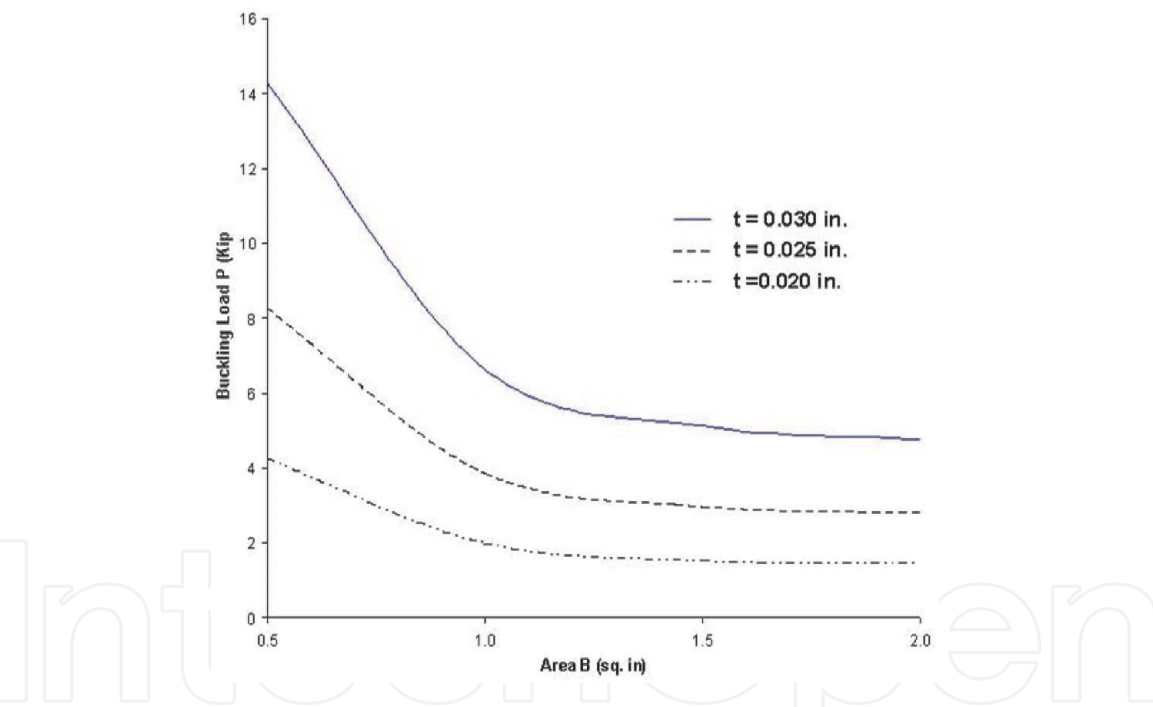


Figure 40.
Design critical loads for gusset under web compression.

design thickness. A horizontal line is finally drawn to intersect with the vertical axis at the critical load.

4. Applications of NDT for timber construction

4.1 Introduction

Shelters represent one of the basic human needs and residential buildings meet this need. References [1, 13, 16, 20] depict the state of deteriorated buildings and the methods used for assessing the status of their structural condition. One could

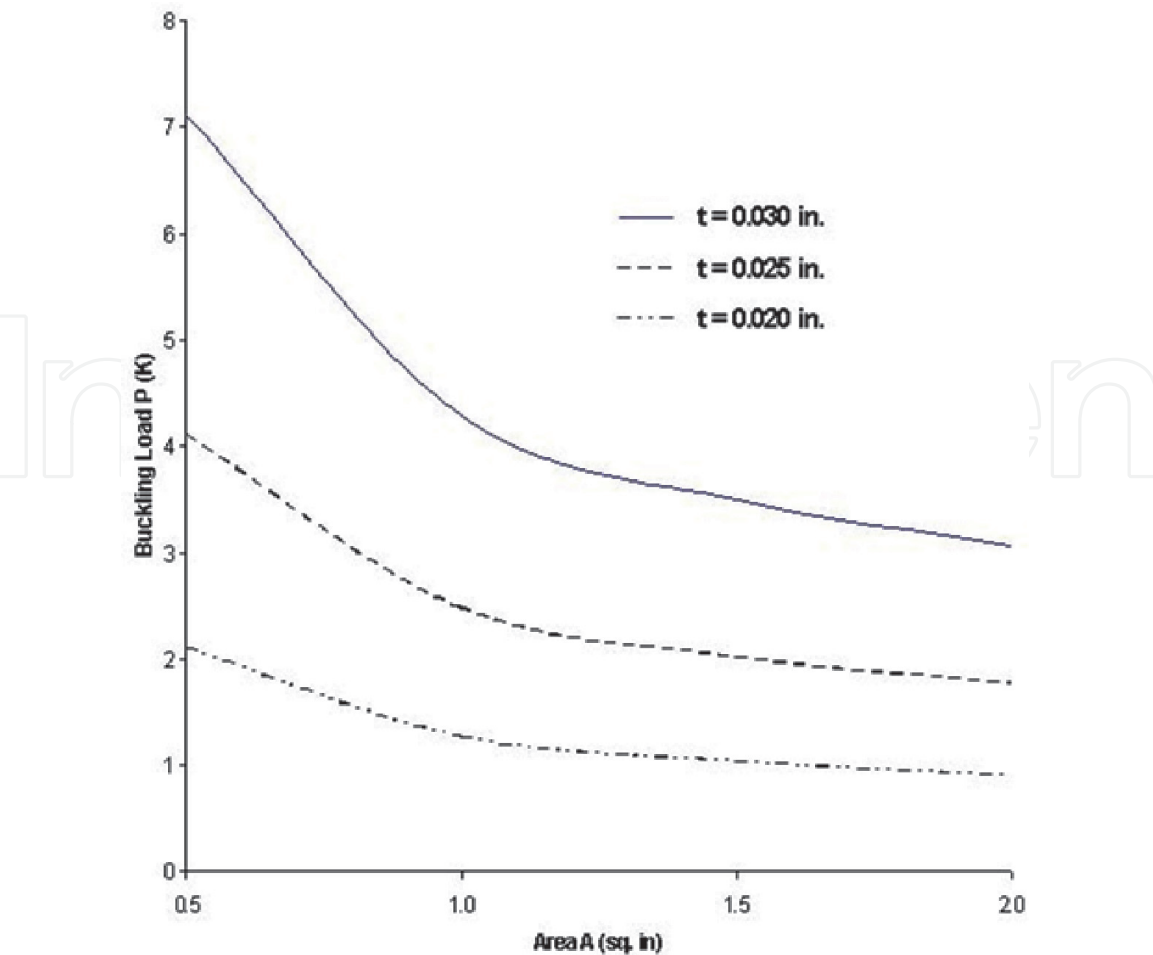


Figure 41.
Design critical loads for gusset joints under chord shear.

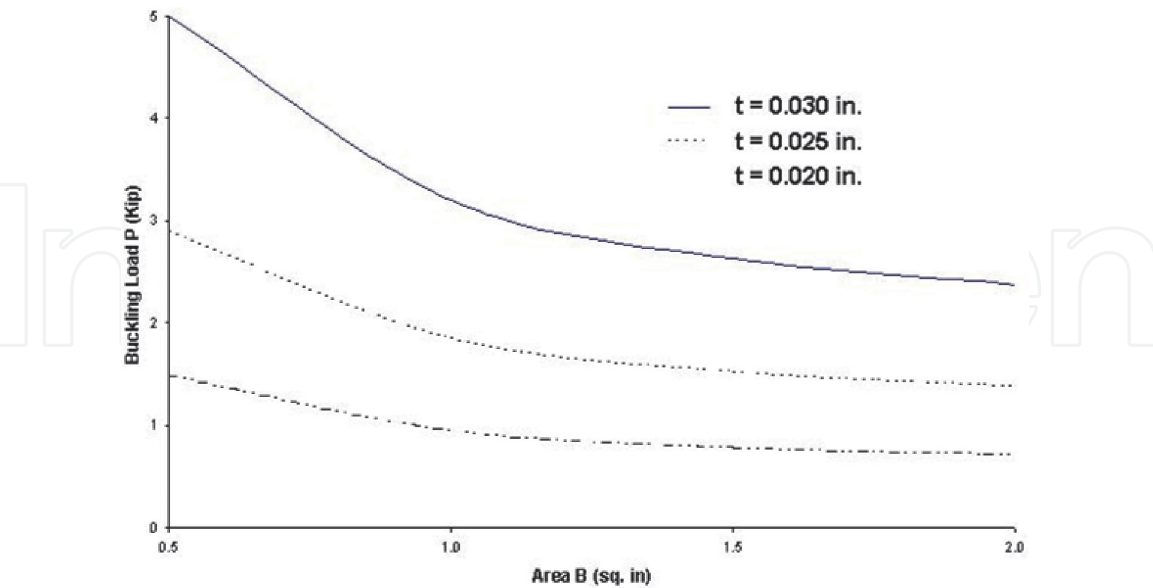


Figure 42.
Design critical loads for gusset joints under chord shear.

see in these sources and many others the complexity of the technical tasks involved in the repair projects.

In general, the need to determine the true structural status of load bearing members is motivated by a number of circumstances such as:

- The existence of defects in the system.
- Damage after natural events such as earthquakes.
- The change in the function of buildings.
- New regulations.

The assessment of the actual structural condition of the load bearing members is a necessary step in all engineering projects. This step is not easy to take because of the architectural configurations and the framing systems. Thus, the assessment of the actual condition of a component comprises in-situ tests and procedures as described by the authority in charge of the projects. In general, tests are expensive and not simple to perform, let alone feasible to conduct. In addition, monitoring procedures are expensive and cumbersome. Thus, non-destructive approaches lend practical ways to overcome these obstacles. From this perspective, a new non-destructive approach has been adopted in this chapter for fast yet reliable outcomes.

4.2 Description of the problem

The engineering analysis and design of construction systems start with analytical models to be solved for the quantities of interest. The models require the geometrical configuration, the applied loads, pertinent mathematical theories or methods, experimental data if needed, and algorithms to execute the procedure. The outcomes are then used for remedial solutions of fragile systems, retrofitting, rehabilitation, etc.

The modeling of old buildings is, in general, more difficult and less reliable than in the case of new buildings. This is due to several factors, such as:

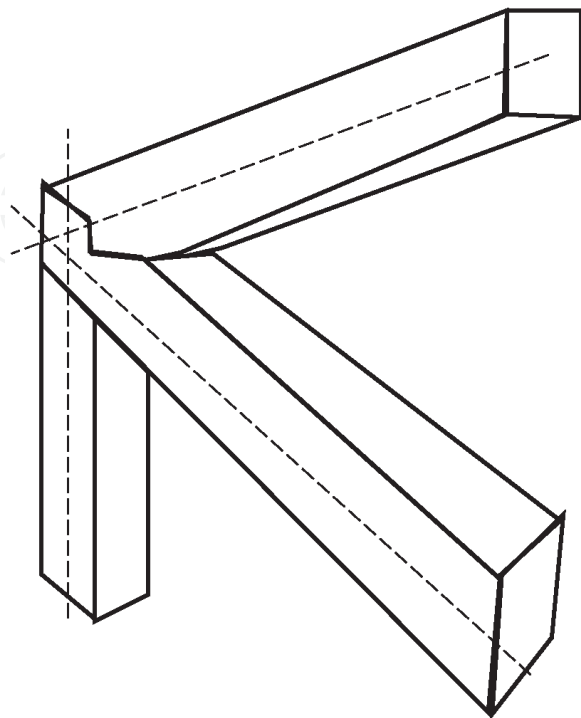


Figure 43.
A typical structural joint.

- The geometrical configuration.
- The uncertainties of the materials properties.
- The invisible impacts of past events such as earthquakes.

Additional factors that compound the analytic modeling include the need for great experience about the structural behavior of building systems, local damages such as cracks, the actual constituent relationships; the alterations over time such as the creation of openings or the removal of components (headers, walls, etc.) or the increase in the height of some spaces, etc. In general, the structural and mechanics procedures are not simple and in most if not all applications require experience. Consider for example, the joint shown in **Figure 43**. In any analytical procedure, it is commonly defined as pin or rigid. Any definition is a mere judgment because true connections are neither of these theoretical cases, and in fact fall in between. The question is: how could a practitioner define the real condition? The answer is essential because the outcomes of the modeling depend on this definition. The rigorous procedure introduced in this chapter contributes to a reliable answer.

4.3 Formulation

To simulate realistically a structural joint, we use semi-rigid connections. Such a joint is neither pin with zero stiffness nor rigid with infinite stiffness. **Figure 44** shows a beam element with end stiffnesses K_i and K_j . The member end forces-displacement and mass relations are expressed in the literature in the form of a 6-by-6 matrices in which the following parameter is used

$$C_i = \frac{L K_i}{E I + L K_i} \tag{55}$$



Figure 44.
Frame element with semi-rigid connections.

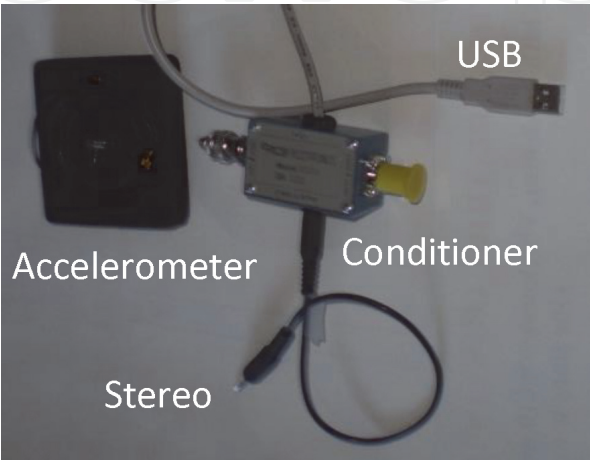


Figure 45.
Signal conditioner.

in which L is the length, I is the sectional moment of inertia, and E is the modulus of elasticity of the material. The structural dynamic governing equations of this are

$$[M]\{\ddot{x}\} + [K]\{x\} = 0 \quad (56)$$

$$|[K] - \omega^2[M]| = 0 \quad (57)$$

where x is the joint rotational displacement, and ω is the fundamental frequency which can be measured using a setup as shown in **Figure 45** in conjunction with FFT analysis.

Once the geometrical and material properties of the member, and the FFT outcome are obtained, Eq. 57 can be iteratively solved for K_i and K_j . The solution process is referred to in the literature as reverse engineering. It is an iterative process in which initial connections are provided then iteratively updated until Eq. 57 is satisfied.

Putting the described direct, easy to perform, and inexpensive procedure together, this chapter suggests the following new complete protocol for the structural assessment of the joint stiffness of an actual frame member:

1. Measure the geometrical properties of the member.
2. Define the elastic properties of the member' material.
3. Use a set up as shown in **Figure 45** to detect dynamic signals on which use FFT.
4. Solve Eq. 57 for K_i and K_j .

To verify the method introduced in this chapter for the assessment of joint stiffnesses, selected data from the literature is used. NASA [1, 17] applied the finite element method, which is an advance method and requires experience, to investigate many joints from pin to fixed conditions, and the results are shown in

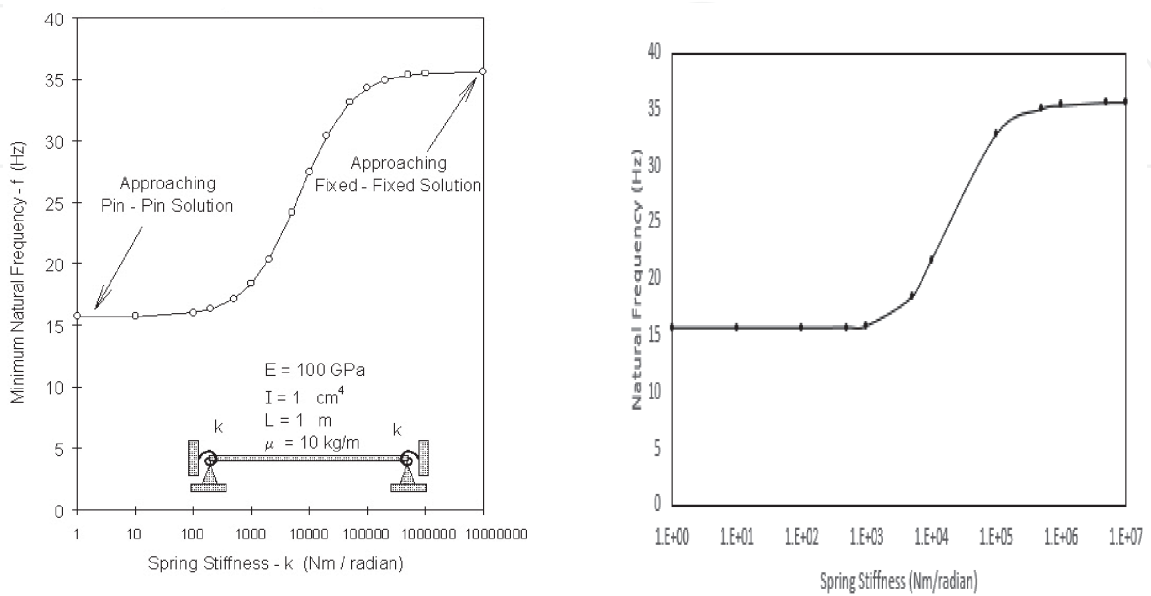


Figure 46. Comparison between the frequency-rotational stiffness relation determined by NASA and this chapter. (a) NASA, (b) This chapter.

Figure 46a. By using NASA's data, we solved the same problems according to our method, and the results are shown in **Figure 46b**. **Figure 46a** and **b** show no significant difference. There was no need for experience and fast results were obtained. This agreement has built confidence in the accuracy and validity of the introduce method and procedure for buildings construction.

5. Knowledge-based cross laminated timber IN building construction

5.1 Introduction

In general, cellulose materials such as timber have been used in construction since mankind started to build shelters. In the broadest sense, timber is characterized by low weight, prefabrication ability, astatic, acoustic properties, and potential recyclability. The mass timber (MTC) refers to framing system in which timber panels are used for the load bearing components. The products in this category includes cross-laminated (CLT) timber, the nailed laminated timber (NLT), the glued-laminated timber, the doweled-laminated timber (DLT), the structural composite lumber (SCL), and the timber-concrete composites [13]. A 2017 study [20] has doubted the MTC's environmental advantages and even if they are known in indiviual construction projects.

According to the CLT Handbook [1], if we perhaps form a hypothesis about likely comparative performance of CLT and assume that CLT has a smaller manufacturing carbon footprint than concrete and steel, it would follow that CLT would perform similarly given that it would have more timber available for landfill storage at end of life. Another study conducted by the Pacific Northwest Building Resilience Coalition [2] in 2018, suggests that the cost of the structural frame for the CLT option is greater than that of the cast-in-place reinforced concrete option, and the concrete in an evaluated ten-story building is less susceptible to floor under dynamic loads, and to excessive lateral drift under wind and seismic loads. The author of this chapter advises caution for judgments when using the available literature. Nonetheless, there are advantages in using timber products but some of the reported disadvantages from MTC include [16] softer materials due to cross laminations, rolling shear, limited dimensions, dimensional stability, fabrication, heavy weights, [17] cost compared to steel and concrete, restrictions on building heights, cost of utilities, cost of design, and cost of transportation. However, as more production and demand will hopefully drive down these costs and increase competitiveness. Some of the factors that affect the environmental benefits of MTC include [20] carbon sequestration rate, timber type, manufacturing processes, material size, equipment and fuel type, regulations, potential of water and insect damages, deconstruction, to name a few examples. The issue of environmental benefits assessment is beyond the scope of this chapter.

Cross laminated timber is an engineered timber category of the MTC and is fabricated by adhering and compressing timber layers in perpendicular grain orientations to form a solid panel. Timber layers are glued together on their wide faces. CLT technology was invented and developed in central Europe in the early 1990's and since then it has been gaining increased popularity in residential and non-residential applications. Recently, CLT was introduced also overseas, in North America, Australia and in New Zealand. A number of production plants have been established or they are proposed to be built in these countries.

The manufacturing process of CLT includes primary lumber selection, lumber grouping and planning, layers cutting to length, adhesive application, panel lay-up, assembly, product curing, surface machining, and marking and packaging. Each of

these steps includes several sub-steps and pertinent details can be found in the literature. The manufacturing requirements are well established and practiced, and available in many international sources in the literature.

The European quality control system requires following specific guidelines for production and testing before obtaining technical approvals. In USA, the American National Standards Institute approved the Standard for Performance-Rated Cross-Laminated Timber. These standard covers manufacturing, qualification and quality assurance. The list of other governing organizations includes the American Wood Council, Canadian Standards Association, International Code Council International Building Code, and the Engineered Wood Association.

Internationally, the list of pertinent organizations includes the International Organization for Standardization, American Society for Testing and Materials, New Zealand Standard Timber Structures Standard, and the European Standards.

5.2 Structural strengths and serviceability

The CLT panels act similarly to sandwich construction. The layers in the longitudinal direction carry the bending stresses whereas the transverse layers provide thickness for high inertia and integrate the layers. In this configuration, the transverse shear is carried by all layers. CLT panels have reinforcing effect for prevention from brittle failure modes such as splitting and increases strength capacity of connections. The cross-laminating process provides improved dimensional stability to the product which allows for prefabrication of long and wide panels. There are different methods to connect the panels to each other such as single or double wooden splines, dowels, and mechanical fastener as nails, screws, bolts, split rings, and shear plates.

At this time, this seed R&D focuses on the development of a KB new toolkits for CLT only using Matlab, Python, and VBA for the CLT structural analysis, calculation, design according to the US standards. The algorithms presented here can be used as a foundation for numerical modeling of CLT structures. This step enables the user to model a CLT structure, starting from the creation of the geometry and the assignation of numeric entities (beam, shell, etc.) to geometric ones, having defined the material, and assigning loads and boundary conditions. This is a seed that will blossom to include other structural components not considered at this time.

The governing formulas for the bending and compression design of CLT are [1, 18, 21, 22, 25, 26].

For bending capacity

$$M_b \leq F_b S_{eff} C_D C_M C_t C_L \quad (58)$$

For shear capacity

$$F_s \text{ or } v(Ib/Q)'_{eff} = C_M C_t F_s (Ib/Q)_{eff} \quad (59)$$

For compression capacity

$$P_c \leq F_c A_{parallel} C_D C_M C_t C_P \quad (60)$$

For deflection under uniform load w

$$\Delta_{max} = \frac{5}{384} \frac{w L^4}{EI_{eff}} + \frac{1}{8} \frac{w L^2}{G A_{eff}} \quad (61)$$

in which

$$S_{\text{eff}} = \frac{0.85 (EI)_{\text{eff}}}{12 E_{\text{major}} t_p}$$

$(EI)_{\text{eff}} = \sum_{i=1}^n E_i b_o \frac{t_i^3}{12} + \sum_{i=1}^n E_i b_o t_i z_i^2$ = Effective flatwise bending stiffness, lbf-in²/ft. (N-mm²/m)

$$(Ib/Q)_{\text{eff}} = \frac{(EI)_{\text{eff}}}{\sum_{i=1}^{n/2} E_i h_i z_i}$$

$$GA_{\text{eff}} = \frac{(t_p - \frac{t_1}{2} - \frac{t_n}{2})^2}{\left[\left(\frac{t_1}{2 G_1 b_o} \right) + \left(\sum_{i=2}^{n-1} \frac{t_i}{G_i b_o} \right) + \left(\frac{t_n}{2 G_n b_o} \right) \right]}$$

= Effective flatwise shear rigidity, in lbf/ft. (N/m) in the major strength direction.

M_b = Applied bending moment.

P_c = Applied axial load.

F_b = Reference bending design stress of outer lamination.

S_{eff} = Effective section modulus.

E_i = modulus of elasticity of the i-th layer, in psi (MPa).

$(EI)_{\text{eff}}$ = Effective bending stiffness.

GA_{eff} = Effective shear stiffness.

C_D = Load duration factor.

C_M = Wet service factor.

C_t = Temperature factor.

C_L = Beam stability factor.

C_P = Column stability factor per the National Design Specifications (NDS).

t_i = Thickness of laminations in the i-th layer, in (mm).

b_o = CLT width in the CLT major strength direction, in/ft. (mm/m).

z_i = Distance between the centroid of the i-th layer and the neutral axis, in (mm). for the middle layer, z_i is to the centroid to the centroid of the top half of that layer.

n = Number of layers.

h_i = Thickness of i-th layer, in (mm).

t_p = Gross thickness of CLT panel, in. (mm.).

A_{parallel} = Area of parallel layers parallel to the load.

K_s = Constant for the effect of shear deformation.

The above governing formulas are recognized and applied in practical applications and used, though the author of this chapter has some reservations, for the development of the unparalleled TLC KB toolkit. The dashboard of the TLC Toolkit is shown in **Figure 47**. Like all other novel toolkits introduced in this chapter, it is user friendly and needs the data highlighted in light green color. Once the user clicks the calculate button, the previous formulas are used to calculate the output shown in the white areas. The outputs are needed to calculate the bending and axial capacities, and serviceability parameter of the CLT. These quantities can then be checked using the limits set by adopted design codes.

CLT CALCULATOR

n	5.000
hi, in.	1.375
Emaj, psi	1,700,000.000
Emin, psi	1,200,000.000
Eleff, lb-in2	440,217,851.563
G Aeff	924,725.275
Fb, psi	1,950.000
Fb Seff, psi	10,405.149
Ib Qeff	54.276
Fs, psi	45.000
Fs Ib Qeff, psf	2,442.404
Ks	11.8
L, in.	240
Fc, psi	1800
Fc Cp A, lb	79,193.881
Load, psf	80
Span, ft	16
Deflection, in	0.308
<div>clearcalculate</div>	

Figure 47.
Dashboard of the CLT toolkit.

6. Knowledge-based toolkits for infrastructure health assessment and monitoring: utility poles/geofoam

6.1 Introduction

Disasters can be prevented or contained by conscious human actions designed. It was this recognition that prompted the author’s conceptual shift from the traditional emphasis on response or resistance (post-actions) to disaster monitoring and prediction (pro-actions) as reflected in this section of the chapter. Our carried out works so far have been shaped essentially by this appreciation. The field of HAM encompasses a myriad of local and global infrastructure problems. This chapter deploys and demonstrates our overall long-term architecture blueprint for a robust health identification and performance monitoring of infrastructure systems.

Taken as a whole, the characteristics of current methodologies place serious limitations on their practical use. Indeed, there are no paradigms of reliable strategies in this field that are robust enough to be of practical use. This section of the chapter will, presumably, revitalize greater and consistent acceptance of our HAM technologies. The ultimate benefit of this is an optimization of both the infrastructure performance as well as costs of repairs to extend the service lives.

Finally, it is important to recognize that although much progress has been made in this field to-date, our understanding of all technical and economic aspects is incomplete. It is anticipated that the technological vision presented herein will serve as a platform from which pertinent advances may be launched leading to more confidence in our infrastructure.

6.2 Structural health condition assessment

In general, the process of health condition assessment and performance monitoring can be categorized into five stages:

1. Identification of damage presence.
2. Localization of damage.
3. Identification of the damage type.
4. Quantification of damage severity.
5. Prediction of the remaining service life.

Customarily, the paradigms for HAM can be depicted as a four-part process:

1. Operational evaluation.
2. Experimental measurements.
3. Relevant data extraction for damage features.
4. Analytic investigation.

Operational evaluation defines why the process is to be performed, tailors its unique aspects of the system and unique features of the damage that is to be identified. The operational evaluation answers four questions regarding the implementation of a HAM system:

1. How is damage defined for the system?
2. What are the conditions under which the system to be monitored functions?
3. What are the limitations on acquiring data in the operational environment?
4. What are the economic and/or life safety motives for performing the monitoring?

Current health monitoring experimental techniques require that the vicinity of the damage is known a priori and that the portion of the structure being inspected is readily accessible. Some of the drawbacks of these methodologies include:

1. The use of expensive instrumentations and data processing hardware not designed specifically for structural health monitoring. The relative expense of these sensing technologies dictates that a structure must be sparsely instrumented
2. Varying environmental and operational conditions produce changes in the system's structural response that can be easily mistaken for damages

These drawbacks place serious limitations on the practical use of existing methodologies. Indeed, there are no HAM paradigms of reliable strategies that are robust enough to be of practical use. Our concept for the future HAM is based on a fresh look at the overall picture. Thus, we divide the future HAM into two categories:

1. Intelligent knowledge-based systems which prognosis potential damages.
2. Existing damage identification and structural performance monitoring.

This new concept emerges from an open-end modular approach that can be adapted to any system, i.e., is not limited to a particular type of damage or material, damage detection or identification techniques. Our HAM will equally perform supervised and unsupervised learning. Supervised learning refers to situations where data from damaged and undamaged structures are available. Unsupervised learning refers to situations where data is only available from the undamaged structure.

6.3 Damage assessment and monitoring

We have been tackling the problems associated with structural health identification and health monitoring. This learning process has evolved and culminated in presenting this part of the chapter. However, because there are several confounding factors and unanswered questions in this field, we embarked on the idea of importing “smartness” to the process. To adequately probe damages, we should search for characteristics such as: the existence of damages, whereabouts of the damaged areas, the type of damages, the size of damages, and the remaining service life in the system.

In answering the above questions, DIM is our promising candidate for HAM utilization. Some of its unique capabilities include the following:

1. DIM's toolkits for damages identification.
2. DIM facilitates the complex HAM process.
3. DIM uses modular architecture which allows for adaptation to new development.
4. IM has a built-in database for most of the available technical information to avoid any incorrect or impractical input data.

7. DIM: geotechnical applications

Under the immense pressure of environmental, energy, economic, and other modern problems, many new materials have been developed from a wide range of renewable, natural, and manmade resources. These innovations meet urgent needs

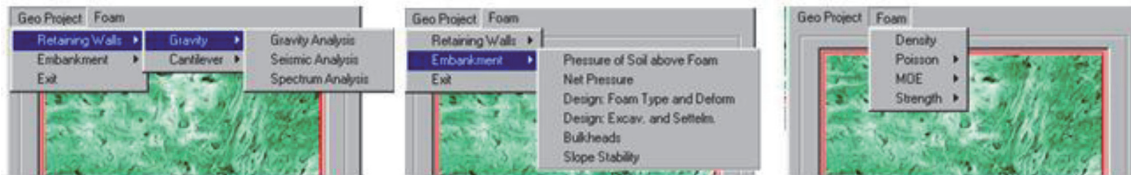


Figure 48.
 Illustrative screens for the DIM' geo client.

such as high strength/weight ratio, thermal insulation, design flexibility, durability, low moisture absorption, ease and speed of construction, and suitability for adverse weather conditions. DIM incorporates a module for the applications of the emerging materials in geotechnical applications such as embankment, retaining systems, foundations (<https://aitechm.wixsite.com/8kbextech>). As shown in **Figure 48**, the scope covers the following:

1. Static.
2. Seismic and spectrum.
3. Slope stability.
4. Strengths.
5. Stress distributions.
6. Uplift and net stresses.
7. Designs
8. Serviceability.

7.1 DIM: biodegradable, bio-based, and synthetic load-bearing components

As elaborated previously, there is no HAM available for the newly emerging load bearing components. The DIM fills this gap and provide many capabilities for biodegradable, bio-based, and synthetic based panels and plates used as load bearing components. It should be noted that the analytical background of this part is presented earlier in the chapter (<https://aitechm.wixsite.com/8kbextech>). The scope of the DIM includes the following, as shown in **Figure 49**:

1. Loads:
 - Different patterns of transverse loads.
 - In-plane loads.
2. Instability:
 - Shear.
 - Uni-axial.



Figure 49.
Illustrative screens for of the DIM' bio load bearing client.

- Bi-axial.
- Local instability.

3. Bonding:

- Rigid bonding.
- Imperfect bonding.

7.2 DIM: utility network grids - poles

Overloading, aging, and environmental impacts are inevitable blows to the utility grids over the lifetime. Unfortunately, these adverse acts result in deterioration. For this specific problem, our overall goal is to develop a specific DIM with the following objectives:

- Determination if a damage is present in the pole.
- Determination of the location of the damage.
- Quantification of the severity of the damage.
- Prediction of the remaining service life of the pole.

Existing pertaining DIM methodologies rely on either visual inspection or localized measurements. Those methods include acoustic measurements and manual sample extraction techniques. Although many of these techniques found applications in the field, there remain some problems that restrict their effectiveness such as:

1. All the techniques require that the vicinity of the damage is guessed a priori and that the portion of the pole being inspected is readily accessible.
2. Contaminating the poles during extraction of test samples.
3. Soil excavation is required; thus, disturbing the supporting conditions.
4. The attachments were never considered in any of the methods.

The adverse impacts of these factors on the use of existing methods were studied by testing 30 real full-scale poles to true failure. The results indicated that none of the available methods was sufficiently accurate as a means for identifying the damages or predicting strengths of poles. Thus, the needs for a new DIM has focused on the development of a practical, fully automated, truly autonomous, human-free, inexpensive, and accurate DIM for in-situ poles.

The underlying principle of our new DIM for poles is that dynamic signatures are sensitive indicators of structural integrity. This reasoning is based on the fact that damages change the dynamic characteristics, and therefore, fundamental measurements can be used to identify and monitor damages. This approach is very attractive for the development of this DIM for poles. We believe that a knowledge-based method is the key for achieving this goal. The new DIM is posed as an inverse problem in which the analytic goal is to find pole characteristics using minimum response information obtained from in situ measurements. This inverse problem is formulated based on the rigor fundamentals of engineering mechanics and structural dynamics and is solved using an implicit redundant representation genetic algorithm. The proposed method is capable of locating and quantifying the severity of damage and remaining strength. Because the damaged parts and their locations are not known beforehand, an iterative solution process is necessary to overcome the difficulties associated with the large number of possible output scenarios. For the first time in the literature, we incorporated vital parameters such as the effects of the surrounding soils, the embedded length of poles, and the attachments. Unlike all the existing methods, our approach neither applies sophisticated numerical techniques as the finite element nor employs the traditional destructive techniques. **Figure 50** shows a selected screen for our DIM toolkit. In situ setup include recording the dynamic signal of poles, FFT analysis of the signals, and integrating the results with the presented analytic method to determine the previously mentioned characteristics of the defective zones.

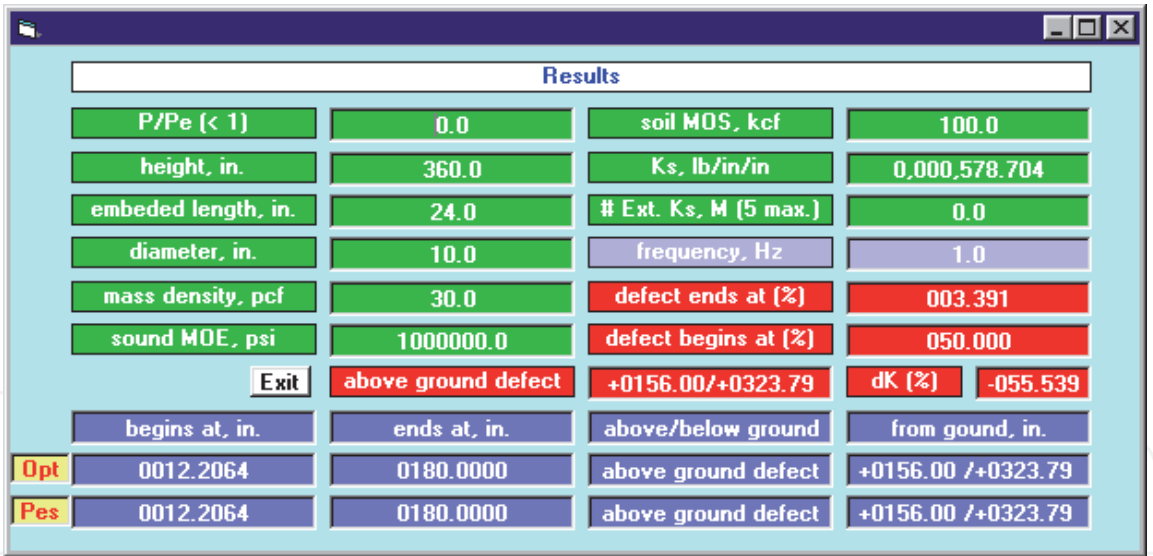


Figure 50.
Illustrative screen for the DIM[®] poles client.

Damage (%)		Frequency		
Begins at	Ends at	FE	DIM	%
95	100	35.9	36.3	1
90	100	23.4	23.7	1
58	70	42.6	43.0	1
Sound pole with overhead		118.3	118.2	0

Table 1.
Comparison of results obtained using the presented technology and FE.

To verify the procedure introduced in this chapter, selected problems were used in conjunction with the previous analytical method. **Table 1** compares the predicted status of selected poles and the corresponding finite element solutions. The table shows very close agreement between the results. This agreement has built confidence in the accuracy and validity of the introduced procedure for utilities (<https://aitechm.wixsite.com/8kbextech>).

7.3 Conclusions

The developments of modern materials and the unprecedented advances of technologies brought to the applications of green laminated composites to the forefront of construction systems. The use of adhesives is unavoidable in manufacturing the panels. However, the assumption of perfectly rigid bonding is very common in the available literature and industries. This assumption is unrealistic because adhesives like all materials have finite properties. This section in the chapter replaced the hypothetical assumption with realistic one. Closed form solutions were presented for load bearing composite panels under flexural and in-plane loads. Unlike the available theories in the literature, the solutions used bonding with realistic stiffness rather than the commonly used perfectly rigid adhesives. The solutions satisfy the equilibrium equations of each lamina, the interlayer deformation and stress compatibility equations, and the panel boundary conditions. To ascertain the effects of bonding stiffness on the performance, numerical results were obtained. The results proved that low bonding stiffness has a strong effect on the laminates deflection. For economical and safety reasons, a new parameter was introduced in the form of core-to-adhesive stiffness ratio. This ratio suggests that very stiff adhesive used in panels with soft core would yield expensive panels and the converse is unwise.

Acknowledgements

This section did not receive funds for its development.

Conflict of interest


The author declares no conflict of interest.

Author details

Rafaat Hussein
SUNY, New York, USA

*Address all correspondence to: ezpsc@gmail.com

IntechOpen

© 2021 The Author(s). Licensee IntechOpen. Distributed under the terms of the Creative Commons Attribution - NonCommercial 4.0 License (<https://creativecommons.org/licenses/by-nc/4.0/>), which permits use, distribution and reproduction for non-commercial purposes, provided the original is properly cited. 

References

- [1] Ahmed M. et. al., Recent Advances in Green Composites, Materials Science Engineering, Vol. 425, 2010, pp 107–166, <https://doi.org/10.4028/www.scientific.net/KEM.425.107>.
- [2] Bujanovic B, SUNY (2018) Personal communication
- [3] Hussein, R. (2019) Artificial Intelligence for Performance and Monitoring of Sustainable Built and natural Environments, and the Climate, Chapter 7, Advances in Artificial Intelligence, the International Frequency Sensor Association.
- [4] Karbhari VM (1997) Application of composite materials to the renewal of twenty-first century infrastructure. Proceedings of the Eleventh Conference on composite materials. Melbourne Australia
- [5] Mohanty A et al (2005) Natural fibers, biopolymers, and biocomposites. CRC Press, Florida
- [6] Rigoberto B et al (2015) Sustainable cellular biocomposites from natural fibers and unsaturated polyester resin for housing panel applications. J Polym Environ 13(2):139–149
- [7] Satyanarayana KG (2007) Biodegradable composites based on lignocellulosic fibers. International Conference on advanced materials and composites (ICAMC)
- [8] The University of Maine (2019) Advanced structures and composite center. <http://www.aewc.umaine.edu/>
- [9] Vanderbilt MD, Goodman JR, Criswell ME (1974) Service and overload behavior of wood joist floor systems. J Struct Eng Div ASCE 100(ST1):11–29
- [10] Placidi L et al (2018) A strain gradient variational approach to damage. A comparison with damage gradient models and numerical results. Math Mech Complex Syst 6:77–100
- [11] Placidi L, Barchiesi E (2018) Energy approach to brittle fracture in strain gradient modelling. Proc R Soc Math Phys Eng Sci 474:878
- [12] Placidi L et al (2018) Two-dimensional strain gradient damage modeling: a variational approach. Zeitschrift für Angewandte Mathematik und Physik 69:56
- [13] Allen HG (1969) Analysis and design of structural sandwich panels. Pergamon Press Ltd, Oxford
- [14] Noor AK et al (1996) Computational models for sandwich panels and shells. Appl Mech Rev 49(3):155
- [15] Plantema FJ (1966) Sandwich construction—the bending and buckling of sandwich beams. John Wiley and Sons Inc, Plates and Shells
- [16] Goodman JR, Popov EP (1968) Layered beam systems with interlayer slip. J Struct Eng Div ASCE 94:2535–2548
- [17] Goodman JR (1969) Layered wood systems with interlayer slip, Wood Sci 1 (3):192
- [18] Goodman JR, Vanderbilt MD, Criswell ME, Bodig J (1974) Composite and two-way action in wood joist floor systems. Wood Sci, 7(1)
- [19] Hussein R (1986) Composite panels/plates—analysis and design. Technomic Publishing Inc
- [20] Allansson, A., "Stability and collapse of corrugated board;" MS Thesis, Lund University, 2001
- [21] Hussein R (2002) Exact closed-form solutions for fiber-fiber and bond-fiber

interactions with imperfect bonding.
Progress in Paper Physics Conference,
Skaneateles

[22] Hussein R (2020) An analytic
solution for fiber-bond interactions, The
116th ESPRA Conference, Bethlehem

[23] Nordstrand, T., "Basic testing and
strength design of corrugated board and
containers," Doctoral thesis, Lund
University, 2003

[24] Hussein, R. (2020) Knowledge-
based Tools for Monitoring and
Management, and Design of the
Engineered Infrastructure Construction
Systems, Chapter 5, Advances in
Computers and Software Engineering,
the International Frequency Sensor
Association.

[25] Huang J, Li K (2008) A new soy
flour-based adhesive for making interior
type II plywood. J Am Oil Chem Soc 85
(1):63–70

[26] Hussein, R. (2020) Knowledge-
Based Expert System Technologies for
the Built & Natural Environments,
<https://aitechm.wixsite.com/8kbextech>.